

Detailed Analysis of the Relationship between Geometry and Airflow in older Chinese Adult Male Nasal Cavities

Sean Read



SAMME
RMIT
Australia
Date

Abstract

Abstract goes here

Dedication

To Mum and Dad, Chris, Coka, Gary, Paper & Leigh

Declaration

I declare that..

Acknowledgements

I want to thank my supervisors, Dr Kiao Inthavong and Professor Jiyuan Tu and my cat

Contents

1	Introduction	10
1.1	Background	10
1.2	Research questions and objectives	11
1.3	Research overview	11
1.4	Thesis outline	12
2	Literature review	13
2.1	Nasal Cavity Anatomy	13
2.2	Geriatric rhinology	13
2.3	Experimental Methods in Rhinology	14
2.4	Computational Methods	14
2.5	Geometric Variations	15
2.6	Fluid dynamics	15
2.6.1	Pressure Drop	15
2.6.2	Wall Shear Stress and Velocity	16
2.6.3	Heat and vapour transfer	17
2.7	Demographic studies	17
2.8	Literature gap	18
3	Model Reconstruction and Meshing	19
3.1	Geometry	19
3.1.1	Introduction	19
3.1.2	Non-invasive Medical Imaging	19
3.1.3	Image Segmentation	20
3.1.4	Segmentation Methods	20
3.1.5	Preparation of Model for Meshing	21
3.1.6	Summary	21
3.2	Meshing	21
3.2.1	Introduction	21
3.2.2	Mesh Types	23
3.2.3	Meshing algorithms	24
3.2.4	Quality	24
3.2.5	Mesh Independence	25
3.2.6	Meshing of the Nasal Cavity	26

4 CFD fundamentals	27
4.1 Fluid Dynamics	27
4.1.1 Mass Conservation	27
4.1.2 Momentum Conservation	28
4.1.3 Energy Conservation	29
4.2 Humidity	30
4.3 Solving the Governing Equations	31
4.3.1 Discretisation	31
4.3.2 Numerical Solution	31
4.4 Setup and Solution of Nasal Cavity Models Used in This Thesis .	32
5 Results	33
5.1 Geometry Variations	33
5.2 Pressure Drop	34
5.3 Wall Shear Stress and velocity	40
5.4 Heat and Vapour Transfer	41
6 Discussion	48
7 Conclusion	52

List of Figures

2.1	Streamlines coloured by velocity from [1]	16
2.2	Velocity contours at the nasal valve from [2]	16
3.1	example of how greyscale values are assigned to pixels in a CT image	20
3.2	Flow chart showing the process by which an anatomical geometry is prepared - with the help of medical imaging software - for solution via CFD codes	22
3.3	geometries of the five cavities used for analysis in this thesis	22
3.4	Example of nasal cavity geometry generation: 3.4a shows an example of the extraction of a 3D model from CT scan data, using, in this case, an open source software package, slicer. Figure 3.4b shows the refined geometry extracted from the CT slices seen in figure 3.4 (a)	23
3.5	Examples of the mesh types described in section 3.2.2	24
3.6	Example of mesh cell with spacing Δx , Δy and angle θ between the grid lines along with high AR triangular and quadrilateral elements	25
3.7	mesh independence test carried out for the largest and smallest of the new models presented in this thesis	25
3.8	mesh of NC06	26
4.1	Fluid moving through the computational domain, the inflow of ambient air must be equal to the air entering the lungs	28
4.2	Flow of heat energy through a 2D element	30
4.3	water vapour moving through a 2D element	30
4.4	representation of mesh discretised with finite volume method	31
5.1	silhouettes of the cavities	35
5.2	Colour coded display of the regional divisions used in tables 5.1, 5.2, 5.3	36
5.3	Representation of the slicing method used for sampling data across the sagittal axis throughout this thesis	36
5.4	area versus distance across the four nasal cavities with a series of examples from the literature	38

5.5	area to perimeter ratio variation with normalised length of the nasal cavity from the nostril inlet to the nasopharynx. This length for each model is: 48yo 8.97cm; 60yo 9.26cm; 64yo 9.60cm; 68yo 9.31cm; 78yo 8.45cm	39
5.6	area versus distance across the four nasal cavities with a series of examples from the literature	39
5.7	Direct comparison of WSS surface contours between all models . .	41
5.8	coronal area weighted average of wall shear stress plotted as a function of distance from the entrance to the cavity across the saggital axis	42
5.9	Velocity contours and wall shear stress values along the perimeter outlines of two cross-sections. The x-axis is the perimeter distance starting from the top apex of each cross-section slice, and moves along the perimeter laterally. One full tracing around the perimeter is defined as 1.0. The dashed line represents the floor of the cross-section opposing its apex, and for the nasal valve, the halfway point 0.5, while for the turbinate cross-section it is 0.7. The y-axis represents normalized wall shear stress 0 – 1.	44
5.10	Flow streamlines (coloured in blue) passing through the left and right chambers of the nasal cavity. Each chambers wall shear stress is shown (coloured in red).	46
5.11	average mass fraction of h ₂ o as a function of normalised saggital position	46
5.12	average ambient temperature as a function of normalised saggital position	47

List of Tables

5.1	sectional volume, according to sections as seen in Figure 5.2 (cm^3)	37
5.2	sectional surface area, according to sections shown in Figure 5.2(cm^2)	37
5.3	Effective diameter $d_{eff} = \frac{4v}{a}$ (cm)	37
5.4	Minimal axial cross sectional area (cm^2)	37
5.5	Variation of pressure drop with flow rate (m/s)	38

Chapter 1

Introduction

1.1 Background

The ageing global population increases the need for investment in geriatrics. One area of particular significance within this field is that of rhinology. A range of dysfunctions and aberrations from the normal functioning of nasal cavities in healthy adults have been observed in the elderly population[3, 4]. For example, the occurrence of respiratory diseases in the elderly is markedly higher than that found in younger populations[5, 3]. It has been suggested that these higher recorded rates is due in part to the impaired air conditioning functionality[4].

The nasal cavities of elderly citizens have been shown by previous researchers to exhibit increased volume[6]. Alterations in histiological function have also been shown[5]. The extent to which functional aberrations are caused by geometric (as opposed to histiological) variations remains unclear[7]. These changes in nasal physiology - and their impact on nasal functionality - need to be investigated further.

Computational Fluid Dynamics (CFD) numerically approximate flow field characteristics for a given domain. CFD simulations give highly detailed results with information covering a range of areas for a given fluid system at a minimal cost. One area in which CFD simulations have been gaining credence is that of biomechanics; many biological fluid systems can be modelled effectively through CFD simulations, allowing for an unprecedented insight into their function.

The use of 3D medical imaging techniques such as computed tomography (CT) scans in collaboration with CFD has facilitated the numerical approximation of fluid mechanism parameters in anatomically accurate models. This allows for more detailed analysis of the effects of topological variations on fluid mechanisms. This capacity for detailed comparison makes CFD simulation an ideal tool for analysing the impact of physiological discrepancies on nasal patency.

To date numerous inter-demographic studies have been carried out using CFD analysis of 3D models reconstructed from CT scan data[8, 9, 10]. These

studies have indicated that factors such as ethnicity and gender are liable to impact on nasal physiology. Previous studies have focused on age[8], however to date these age related studies have all focused on children. The use of CFD to examine functional variations in older models - accounting for potential inter-demographic variations such as gender or ethnicity - is thus an important step that needs to be taken in order to achieve a more comprehensive understanding of the impact of ageing on nasal patency.

1.2 Research questions and objectives

In light of the information posed above, the following questions become pertinent:

- How do variations in nasal cavity geometries in older Chinese Males influence the inhaled airflow mechanisms, contributing to respiratory ailments?
- How do the geometry variations impact on heat and vapour transfer within the cavity, contributing to respiratory ailments?

To address these issues, the following objectives are outlined:

- Reconstruct a series of nasal cavity geometries from medical scans that represent a spread of geometric characteristics [such as volume and surface area] across the norm. The existing literature shows a clearly defined relationship between age and volume: these models will serve as a representative sample of the older population to be analysed computationally.
- Model airflow across the series of reconstructed nasal cavities using CFD with a steady state assumption; defining inlet conditions to approximate a resting rate of respiration.
- Compare the simulation results between geometries. A variety of post processing methods are available to compare various aspects of fluid mechanic functionality of nasal cavity models. The literature has shown clear discrepancies in the functionality of nasal cavities as a function of age; it is our intention through these measurements to examine in more detail the relationship between these variations and geometry.
- Compare with results from the literature.

1.3 Research overview

Medical image reconstruction technologies now allow researchers to reconstruct highly detailed, digital 3D representations of various anatomical structures from CT scans. When coupled with CFD simulations, this presents an unprecedented capacity for in depth analysis of physiological fluid flow mechanisms.

This study aims to use CFD analysis of CT scan data from the nasal cavities of a range of Asian males to investigate the impact of geometric variations between older nasal cavities on the airflow structures and air-conditioning capacity of the nasal cavity. Air flow mechanisms, heat transfer rates and humidification efficacy are analysed in order to arrive at a more precise understanding of the role of nasal geometry in the presentation of respiratory ailments.

This study represents, to the best of our knowledge, the first in depth, mechanistic, computational study undertaken into the role of nasal geometry in common rhinological symptoms observed in older patients.

1.4 Thesis outline

Herein a concise description is given of the thesis chapters' contents

Chapter 2 reviews current literature related to the topic at hand. This is divided into sections such as nasal anatomy, rhinology and fluid dynamics. On the basis of this review clear research questions are determined and salient research methods developed.

Chapter 3 provides a detailed description of the process by which anatomical structures are modeled for CFD analysis and the technologies involved. The process by which the models are then approximated by computational meshing - as to make them solvable by CFD methods - is then described

Chapter 4 describes the basic principles of CFD, and how they are implemented for the solution of fluid systems defined by 3D models of nasal cavity geometries.

Chapter 5 presents the results of numerical simulations carried out for a series of older nasal geometries. The results show relationships between cavity geometry and wall shear stress as well as pressure drop. Heat and vapour transfer capacities are also presented.

Chapter 6 discusses the significance of the results presented in the previous chapter. It is postulated that the preliminary understanding of the relationship between age, geometry and airflow dynamics presented in this thesis could help to further our understanding of olfactory mechanisms in the human nasal cavity.

Chapter 7 Summarises the key findings gleaned from this thesis and discusses possible future extensions and applications.

Chapter 2

Literature review

2.1 Nasal Cavity Anatomy

2.2 Geriatric rhinology

The common rhinological complaints of the elderly include dryness, runny noses, crusting and epistaxis[7]. Epidemiological studies have been carried out to examine the consistency of the manifestation of various symptoms throughout elderly patients with mixed results.

The literature at present seems to be unanimous on the tendency of the nasal cavity's cross sectional area to increase with age. Several researchers have investigated this phenomena using acoustic rhinometry and shown good concordance in study outcomes[6, 3, 11, 4]. Loftus et al. [12] compared the volumes of 22 nasal cavity models taken from CT scan data, and also found a clear tendency towards increased nasal cavity volume with ageing. Nasal air heating and humidification examined *in vivo* have been shown to be impaired by ageing[4].

Increases in postnasal drip, nasal drainage, sneezing, coughing, olfactory dysfunction and gustatory rhinitis with age were observed in a clinical study of 131 patients[3]. The results on the impact of aging on the quality of life have not been unanimous, a 2009 study found that in a sample of 80 people no significant relationship could be observed between age and nasal discomfort[13]. The same study, however, concurred with previous results on the increase of volume and cross sectional area as a function of age. Changes within the nose appear to not be limited to the increased volume; Both functional and structural variations in the respiratory epithelium have been observed with age, contributing to slower clearing of mucous[5].

Functional variations in air conditioning capabilities have been shown *in vivo*[4], with statistically significant reductions in relative humidity and heat transfer observed in elder nasal cavities. The level to which this is attributable to change in histological function as opposed to variations in the fluid mechanisms

as a result of the expansion of the cavity remains to be investigated.

2.3 Experimental Methods in Rhinology

To understand more precisely the air flow mechanisms in older nasal cavities, an experimental technique for the investigation must first be chosen. In this section the methods available for investigating nasal patency are presented.

The anatomy of the nasal cavity was first classified in detail by Emil Zuckerkandl in the 19th century[14]. Anatomically, his records were more or less up to the standard of what can be assessed from modern scanning techniques[14], however the investigation of airflow characteristics was still severely limited by technological capacity[15]. It was not until the turn of the 19th century that experimentation into nasal airflow began in proper[15].

Some of the more common *in vivo* techniques used include rhinomanometry, which allows measurement of the pressure drop across the nasal cavity[16] and acoustic rhinometry, which allows measurement of the cross sectional area of the nasal cavity as a function of depth[16].

Ultimately, however, direct detailed measurements of flow mechanics within the human nasal cavity taken *in vivo* are not practically viable with current technology as a result of the complexity and small scale of the nasal geometry[17]. Thus the preferred media for the testing in modern times has tended to be either physical or computational models reconstructed from CT scan data[17]. The physical models that have been constructed from CT scan data are able to provide detailed geometric reproductions. These allow for much more detailed flow analysis when compared with older techniques such as rhinomanometry[18]. Such experimental set ups are, however, costly to run in terms of time and resources, in particular when compared with the high level of detail that can be achieved from a well done CFD simulation[18].

2.4 Computational Methods

Computational fluid dynamics(CFD) is a discipline which is concerned with the computational approximation of solutions to the navier stokes equations for closed fluid systems[19]. In many fields - including rhinology - CFD has facilitated economical and detailed investigations into cases in which experimental investigation would otherwise be costly or impossible[20].

CFDs were the primary driving force behind the development of larger and faster computers until the 80's[21]. In more recent times, the continuing advancement of computational technologies has facilitated considerable growth in the scope and accuracy of CFDs for predicting the behaviour of increasingly complex systems[19].

One of the areas of investigation that has been facilitated by these advances is that of nasal airflow. Initially, simplified nasal cavity geometry models were used to create computational meshes and solve numerically for the fluid flow

characteristics under steady state conditions[20, 22]. Later 3D models extracted from CT scans were used to achieve more accurate results[23]. In addition to this, various inlet and outlet conditions have been considered, including the difference between unsteady state (flowrate as a function of time throughout the nasal cycle)[24] and steady state (constant velocity, time independent) assumption based models[2]. This discrepancy has been a point of much contention, and it seems that the current position is that the correct choice depends on the application at hand[17]. Certainly to date it seems that the vast bulk of the case studies comparing different geometries have used the steady state assumption[8, 10, 9]

Another issue which has been of some debate in the literature is the relevance of the inclusion of sinuses in the modelled flow domain. It has been reasonably commonplace to include the sinuses in studies that are examining the effects of sinus surgery[25, 26]. Also it has been shown that, while the impact on airflow is relatively minimal, the sinuses can be subject to significant levels of particle deposition for particles in the range of 1 nanometre in diameter, and particularly for low flow rates[27]. The added requirements in time and computational complexity necessitated by the inclusion of the sinuses, however, seems to warrant their exclusion from models in situations where they are not specifically relevant[17].

2.5 Geometric Variations

The basis of any in depth investigation into the relationship between geometric variations and airflow structures is a clear analysis of the geometric variations. Cross sectional areas have been graphed as a function of radial position to compare the geometries of different models in many studies[8, 10, 4, 9]. Surface area has also been suggested to be significant metric in predicting flow behaviour (as surface area to volume ratios are expected to impact on the flow behaviour[8, 9]). The minimum coronal cross-sectional area is a figure that has been suggested to be of particular significance to flow development[4]. The ratio of area to volume (or perimeter length to cross sectional area) has been used by several researchers to predict flow characteristics[8, 9].

2.6 Fluid dynamics

2.6.1 Pressure Drop

The earliest papers investigating nasal patency focused primarily on the pressure drop over the nostrils, as measured with rhinomanometry[28]. Resistance across the nasal cavity, measured as pressure drop, is still often used as a predictor of flow behaviour within the nasal cavity[3, 4, 11]. Pressure drop has also been suggested to provide an insight into the inspirational efficiency of the cavities[29]. It is often plotted as a function of flow rate in order to provide a point for validation by comparison with experimental set ups[2, 30]. In addition,

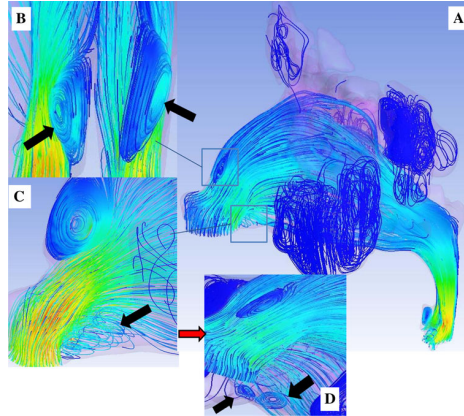


Figure 2.1: Streamlines coloured by velocity from [1]

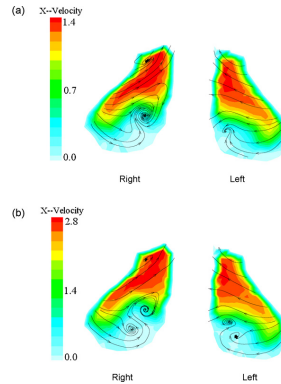


Figure 2.2: Velocity contours at the nasal valve from [2]

it can be treated as a function of longitudinal position in order to gain an insight in to the relationship between the geometric variations and pressure drop[29].

2.6.2 Wall Shear Stress and Velocity

Another important variable is velocity distribution[20, 10, 29]. This can include cross sectional zone by zone analysis[20, 10], which has been suggested to be useful for the measurement of the efficacy of olfaction[10], or by longitudinal sections[29, 31] . Another commonly used quantitative measure is wall shear stress. Distributions are analysed longitudinally[2] or around the cross sectional parameter of the relevant section of the nasal cavity[32]. These measurements have been shown to be significant for predicting heat and mass transfer characteristics[31], and as such their longitudinal and parametric distributions are significant for understanding the distribution of such mechanisms.

One commonly used visualisation method is the use of streamlines (shown

in figure 2.1). Streamlines, often coloured by velocity[2, 10, 9]. These are useful for showing flow distribution as well as significant recirculation zones[29, 33]. Another commonly used method, shown in figure 2.2 is coronal cross sectional contours portraying velocity. These contours may or not include streamlines to help highlight the presence of vortices in the flow[2]. Another method, presented in [29] uses a vortex detection algorithm to trace the vortices present in the flow structure. In [29], these are then coloured by variables related to turbulence and vorticity in order to provide a deeper insight into the vortex structure and behaviour.

2.6.3 Heat and vapour transfer

Earlier investigations into the heat and vapour transport characteristics of the nasal cavity used a straight pipe model as a simplification of the nasal cavity geometry[34]. The first experiments involving real nasal cavity geometries were carried out in the 80s, using cast models taken from cadavers[35].

In vivo experiments into temperature variation across the nasal cavity have been done using various temperature measuring devices; modern experiments have tended towards using thermocouples because they are small and respond quickly[36]. For measuring humidity in vitro, modern researchers have tended towards the use of capacitative humidity sensors[37]. Detailed profiles of temperature and humidity throughout the nasal cavity have been presented by several past researchers[37].

CFD's have been used to simulate heat and vapour transfer in the nasal cavities with good accordance with experimental results[38]. Early simulations investigating heat and vapour transfer used a steady state assumption for inflow conditions[39]. Later, the effect of the nasal cycle on temperature distributions was investigated, showing significant variations in the nasal temperature distributions throughout the nasal cycle[40].

Cross sectional temperature contours have been used to visualise the distribution of temperature throughout the nasal cavity; this provides a clear method visualising the distribution[41]. Saggital heat flux contours have also been used to similar effect[42]. Heat flux, temperature, water flux and humidity have all been mapped as functions of position across the saggital axis in the nasal cavity[9, 42, 43]. The nasal valve has been noted from these observations to be a region of particular significance to heat and vapour transfer mechanisms[42].

2.7 Demographic studies

One of the significant benefits of CFDs in rhinology is the ability to investigate the effects of interdemographic variations in nasal geometry on flow features. The previously investigated demographics include ethnicity[10]; disease[9]; and age[8]. Age can be subclassified into children[8] and the elderly[4]. Both child and older nasal cavities have been investigated through in vitro[44] and in vivo[6, 3, 11, 4] experimental techniques. Child models have also been investigated

computationally[8]. The variations that have been observed in children’s nasal airway functionality has been suggested to be linked to particle filtration ability [8]. It seems plausible that this effect could be significant also in the case of elderly models. It is to date, however, unknown as in depth computational studies investigating flow field variations in older models are yet be undertaken.

2.8 Literature gap

Geriatric rhinology is an area which is growing in significance as the global population ages. Although various experimental techniques have been used historically in rhinology, non of them provide the same cost effectiveness and level of detail which can be obtained through computational analysis of 3D models obtained from medical imaging. This method has been used extensively in recent years to examine interdemographic variations in nasal cavity functionality. To date, to the best of our knowledge, the investigated demographics have not included older patients.

Chapter 3

Model Reconstruction and Meshing

3.1 Geometry

3.1.1 Introduction

The reconstruction of nasal cavity model computer images - including discretisation - can be divided into 5 stages: image acquisition, data conversion, segmentation, refinement and meshing. Firstly medical imaging technologies are used to extract a series of pixelated slices, in which the various materials which make up the human body can be identified by variation in greyscale measurements. These slices are then interpolated to create a 3D structure of voxels (the 3D equivalent of a pixel).

The reconstruction of the nasal cavity geometries can be very time consuming and prone to human error. The improvement on and automation of the reconstruction process are areas of active research. This chapter presents an overview of the methods in current use for the various phases (mentioned above) by which a nasal cavity geometry is prepared for computational solution.

3.1.2 Non-invasive Medical Imaging

There are various forms of medical imaging that can be used for the identification of the nasal cavity geometry. Here we briefly overview Computed Tomography (CT), the form of medical imaging used for the nasal cavity geometries presented in this thesis.

CT scans use a series of x-rays taken at regular intervals within the region of interest. x-ray scans use photons sent in beams through the region of interest; these photons interact differently with the material that they encounter depending on its density. Electronic detectors feed the photon pattern emitted from the body in question to a computer, which uses this information to create

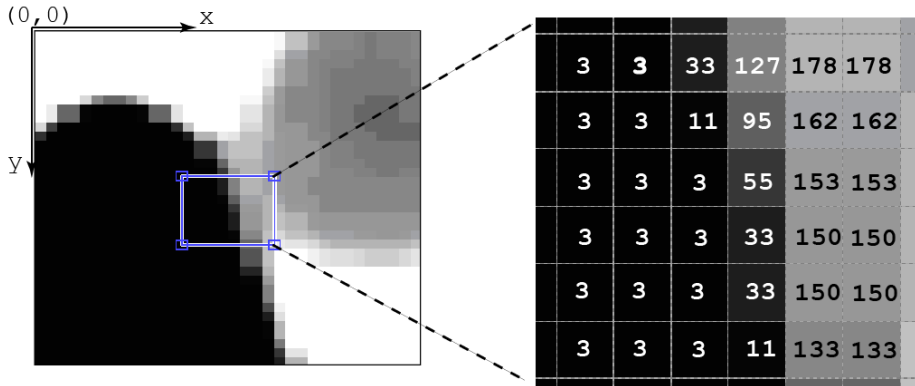


Figure 3.1: example of how greyscale values are assigned to pixels in a CT image

images. These images are made up of pixels which are each assigned a grey scale value based on their x-ray attenuation coefficient. In medical imaging the Hounsfield scale is used, whereas in image processing the greyscale is numbered from black to white between 0 to 255. Figure 3.1 shows an example of how greyscale values are assigned to pixels in a CT image.

3.1.3 Image Segmentation

Once the CT scan has been outputted as a series of voxels, the anatomical geometries relevant to the project at hand need to be extracted. To achieve this goal, the voxels that make up the relevant section of the data need to be identified somehow. This can be done manually - by going through the many slices that make up the CT scan and identifying the relevant areas - however this process is extremely time consuming.

3.1.4 Segmentation Methods

Numerous algorithms have been developed for the purpose of automating the process; all of which have certain advantages and disadvantages. For the most part these algorithms can be subsumed in to three categories, presented below (in order of increasing complexity):

Thresholding regions are identified and separated according their greyscale value. This is the simplest algorithm for defining regions.

Edge detection either local maxima of the first derivative of intensity or zero values of the second derivative are used to identify region edges. Edge detection tends to reduce the noise when compared with thresholding.

Region based regions are grown from the inside out. This produces more coherent regions, but is unable to detect regions that are segregated.

These methods and many more exist and are in active development; many of them are available for free online. The implementation of such algorithms from first principles, however is quite a complex procedure. Fortunately many of these algorithms have already been implemented in software packages - of which commercial and open source variations are available - which are specifically compiled for working with medical imaging outputs.

3.1.5 Preparation of Model for Meshing

Once the region in question has been extracted from the medical imaging output, it can be saved as some CAD format. There are certain criteria that need to be fulfilled by a CAD model before it can be read by 3D meshing software and used to create a mesh. It is often the case when the data is exported from the medical imaging software that it is 'dirty'; that there are contradictory or arbitrary elements in the geometry. These elements need to be removed through the use of CAD software before the geometry is suitable for the creation of a useable 'clean' 3D mesh. Note that the geometry needs to contain also topological information in order to create a watertight mesh. The details of the process by which the geometry is prepared for meshing are described in Figure 3.2.

3.1.6 Summary

Anatomical geometry reconstruction - including that of the nasal cavity - begins with medical imaging of the area in question. The geometry is then extracted from the medical imaging data using one (or several) of the available extraction algorithms outlined above. After extraction, cleaning of the geometry with CAD software is generally necessary to ensure that the geometry is water-tight and 'clean' before it can be meshed. This chapter has given an overview of some of the more pertinent methods in current use for the reconstruction of anatomical geometries from medical imaging data. Figure 3.4 shows an example of the construction process.

Figure 3.3 shows the models reconstructed for and used in this thesis. They have been labeled NC for nasal cavity plus a number. The first cavity, NC04, is 48 years old and was reconstructed by a colleague earlier and used in this thesis as a comparison point for the older models. The other models are aged between 60 and 78. All of the models are of healthy Asian males. In this case we chose only healthy Asian males as to minimise the impact of demographic variations other than age on the presented geometries.

3.2 Meshing

3.2.1 Introduction

The navier stokes equations, upon which CFD is based (see chapter 4), is unsolvable (in most instances), except by approximation. In order to approximate a solution to a given system, its geometry must be approximated, or discretised,

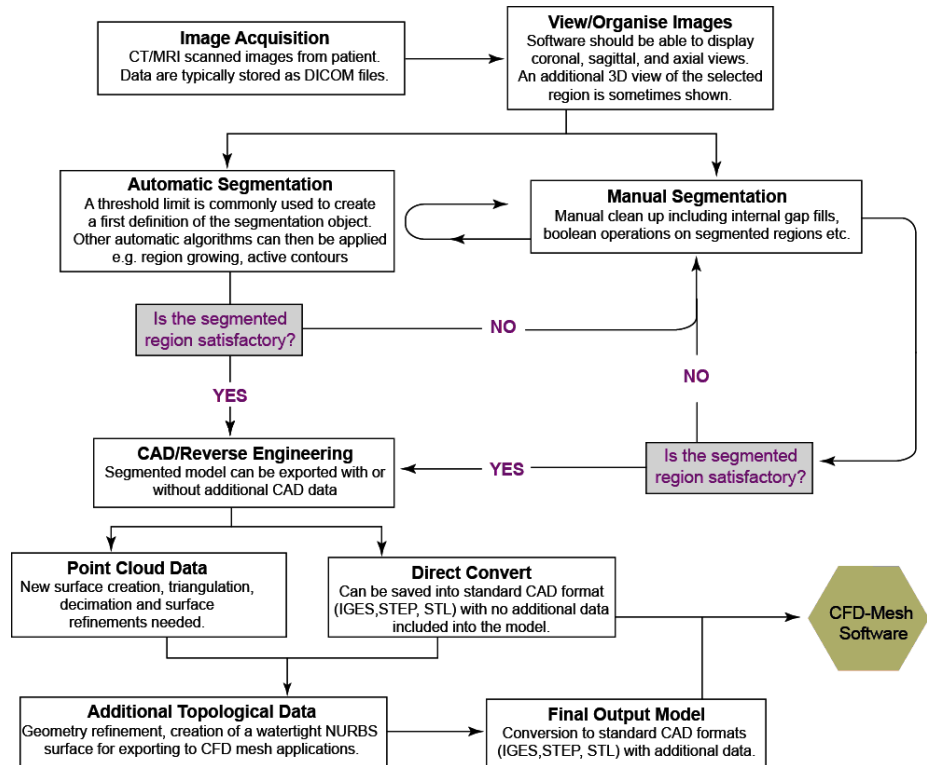


Figure 3.2: Flow chart showing the process by which an anatomical geometry is prepared - with the help of medical imaging software - for solution via CFD codes

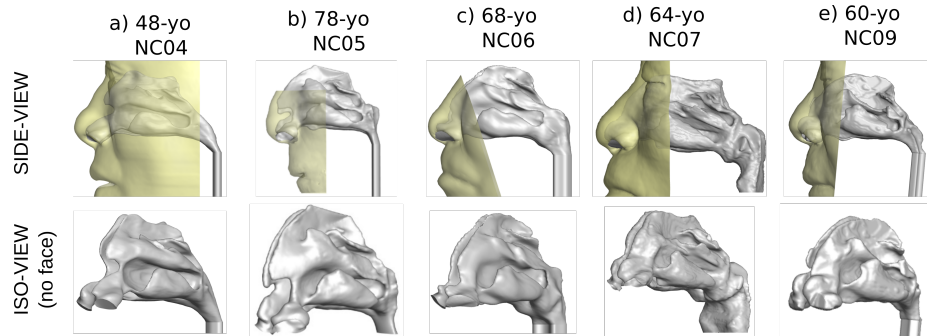


Figure 3.3: geometries of the five cavities used for analysis in this thesis

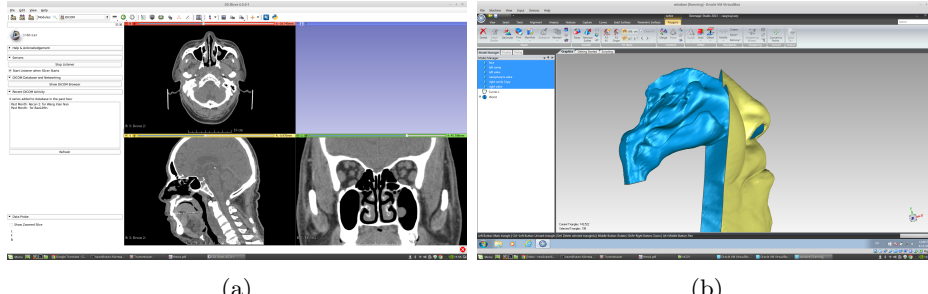


Figure 3.4: Example of nasal cavity geometry generation: 3.4a shows an example of the extraction of a 3D model from CT scan data, using, in this case, an open source software package, slicer. Figure 3.4b shows the refined geometry extracted from the CT slices seen in figure 3.4 (a)

as a series of points. The process by which these points are defined and related to one another is known as meshing; this in itself is a complex discipline under active research. In this chapter current methods are reviewed, and guidelines are given for developing quality meshes.

3.2.2 Mesh Types

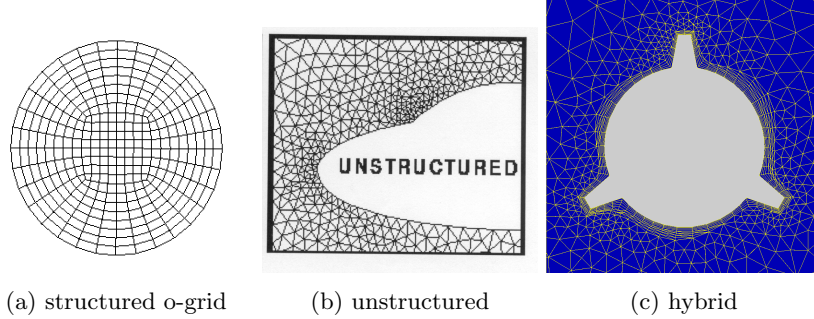
There are many types of mesh that can be employed; all of them have their own advantages and disadvantages.

Structured meshes are divided into segments of uniform size and shape.

They are characterised by cells possessing either four nodal corner points in two dimensions, or eight in three dimensions. The points are mutually orthogonal and cartesionally defined. Being defined in this relatively simple way facilitates a higher level of computational efficiency. They are, however, limited in the level of structural complexity that they can accomodate.

Unstructured Meshes The geometries encountered in the respiratory system are generally too complex to be effectively discretised in a structured manner; in cases such as these unstructured meshes can be used to accomodate the complexities of the given geometry. Unstructured meshes - usually constructed from triangles or tetrahedra - do not fit a regular pattern, and they do not have coordinate lines corresponding to curvilinear directions. Because of this, the solving of computations over unstructured domains is generally more computationally intensive; however with modern advances in computers this has become less significant an issue in many cases.

Hybrid meshes One disadvantage to the use of unstructured meshes is that they tend to show less accuracy near the wall. One commonly applied



(a) structured o-grid (b) unstructured (c) hybrid

Figure 3.5: Examples of the mesh types described in section 3.2.2

solution is the use of hexahedral elements near the wall, with the rest of the volume filled with unstructured - usually tetrahedral - elements. This method tends to improve the accuracy of near wall computations. One draw back of this method is that the prism layers can break down in the vicinity of excessively contoured walls. In this study this is the mesh type that is employed.

3.2.3 Meshing algorithms

There are various meshing algorithms available, each with its own strengths and weaknesses. For the purpose of this study, an octree algorithm was selected. Octree algorithms work by repeatedly dividing The volume in to smaller sections, until the given criteria, for example mesh size, is fulfilled. This method is generally considered to be a relatively simple but robust approach to mesh generation. One drawback, however is that it can cause irregular element distributions near the boundary.

3.2.4 Quality

The quality of a generated mesh is dependant on its warp angle, skewness and aspect ratio. For a quadrilateral cell, as shown in figure 3.6, the aspect ratio of the cell is defined as $AR = \frac{\Delta y}{\Delta x}$. Within the interior region, the AR should be maintained within the range $0.2 < AR < 5$. This can be somewhat relaxed, however, in the vicinity of the wall.

Mesh skewness is defined as the extent to which it deviates in shape from the ideal. This is a square for quadrilateral cells, or an equilateral triangle for triangle or tetrahedral cells. It is defined for triangles and tetrahedrals as $\frac{\theta_{ideal} - \theta_{actual}}{\theta_{ideal}}$ (see figure 3.6 for theta).

Many grid generation packages contain specific algorithms and/or functions for improving mesh quality. The gradient of mesh size variation should not exceed 1.2, as higher variations can cause problems in convergence.

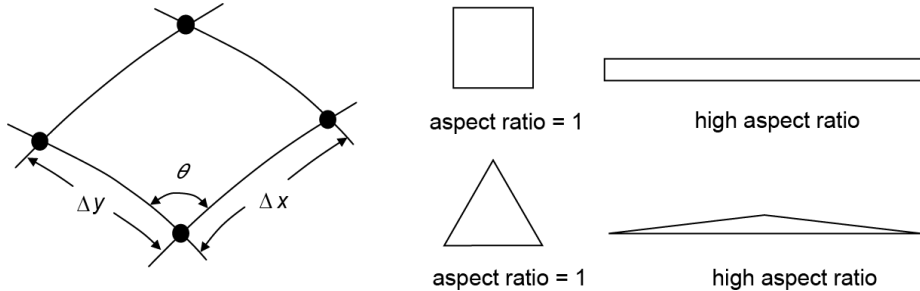


Figure 3.6: Example of mesh cell with spacing Δx , Δy and angle θ between the grid lines along with high AR triangular and quadrilateral elements

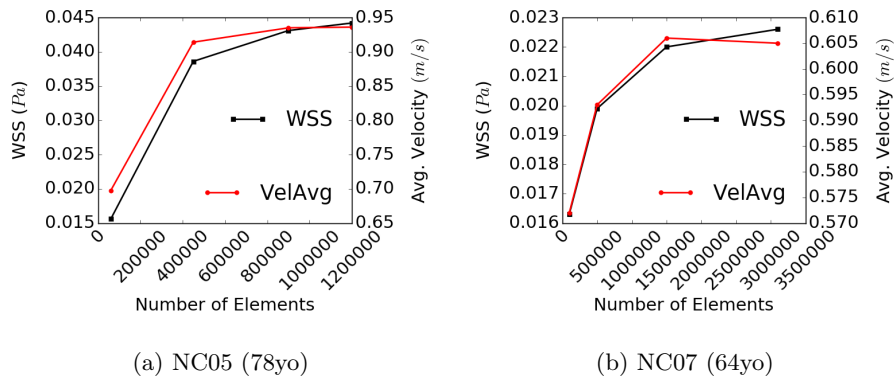


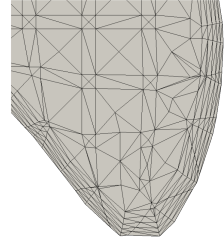
Figure 3.7: mesh independence test carried out for the largest and smallest of the new models presented in this thesis

3.2.5 Mesh Independence

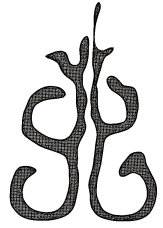
A significant source of error in the solution of CFD problems is derived from the discretisation process; when a system is separated into a number of finite elements, for the purpose of Numerical solution, the solution that is obtained from its solution is an approximation. It is necessary, then, to ascertain the required resolution, or mesh size, required to calculate a result that approximates the exact solution to a satisfactory degree of accuracy. This is done by means of a mesh independence test. This entails the monitoring of one - or several - fluid flow parameters of interest to the study over a series of mesh resolutions for the relevant system. Independence is said to have been achieved when the effect of mesh size on the selected flow variable(s) has become sufficiently insignificant. Figure 3.7 shows the results from the mesh independence test conducted for smallest and the largest of the five models presented in this thesis.



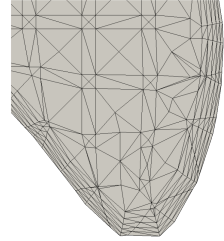
(a) whole system with face, extension from outlet and external zone



(b) intersection of three mesh resolutions



(c) cross section of cavity mesh



(d) prism layer of cavity mesh

Figure 3.8: mesh of NC06 (68yo)

3.2.6 Meshing of the Nasal Cavity

Here we provide an overview of the meshing process applied to one of the nasal cavity models presented in this thesis. The process was the same for the other four models.

The system is divided into three parts. The first of these surrounds the facial geometry directly adjacent to the nostrils; this is to allow for the development of a more realistic inlet profile. The second is the nasal cavity itself. The third section is a pipe-like extension from the exit of the nasopharynx; this allows for the development of a more realistic outlet profile, in a similar manner to the section around the inlet. This system can be seen in Figure 3.8 (a).

The three stages of mesh refinement can be seen in Figure 3.8 (b); The mesh resolution is much coarser in the external domain, refined closer to the inlet and then is most fine in the cavity itself, the area of interest. Note the use of hybrid mesh, with internal tetrahedral elements and close to wall prism layers, shown clearly in Figure 3.8 (d).

Chapter 4

CFD fundamentals

4.1 Fluid Dynamics

The aim of Computational fluid dynamics is to approximate numerically the physical conservation laws of newtonian physics:

- conservation of mass
- The conservation of momentum (Newtons second law, the rate of change of momentum equals the sum of forces acting on the fluid);
- The conservation of energy (first law of thermodynamics, the rate of change of energy equals the sum of rate of heat addition to and the rate of work done on the fluid).

4.1.1 Mass Conservation

The principle of conservation of mass is that, in a closed system, the mass remains constant. This means that fluid will move through a set region in such a way the mass is conserved. For an incompressible flow, this means that the outflows and the inflows will be equal. This can be written as

$$0 = \sum_{in} \dot{m} - \sum_{out} \dot{m} \quad (4.1)$$

Where \dot{m} = mass flow rate.

The mass flow rate can be written as $\rho u A$, for ρ = density, u = velocity and A is the scross sectional area of the flow. For flow in the x direction, $A = \Delta z \Delta x$. For a two dimensional flow, $\Delta z = 1$, giving:

$$\dot{m}_{in} = \rho u \Delta y \quad (4.2)$$

Extending this to equation 4.1, in the x direction, for an incompressible flow we get

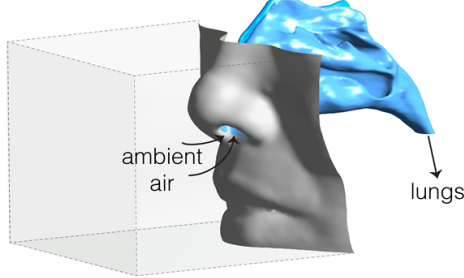


Figure 4.1: Fluid moving through the computational domain, the inflow of ambient air must be equal to the air entering the lungs

$$0 = \rho u_{in} \Delta y_{in} - \rho u_{out} \Delta y_{out} \quad (4.3)$$

This can easily be extrapolated to three dimensions. In the case of the nasal cavity, this can be conceptualised in relation to the nasal cavity geometry, where the air flow rate going in to the nostrils must be equal to that leaving through the extension from the nasopharynx, as seen in figure 4.1.

4.1.2 Momentum Conservation

Momentum conservation is based on the Newton's second law:

$$\sum F = ma$$

Here m is the mass of the system, a is its rate of acceleration, and $\sum F$ is the sum of forces acting on the system. F can generally be divided into body and surface forces. Rewriting the mass as the product of volume and the density, and acceleration as the first derivative of velocity:

$$\sum F_{body} + \sum F_{surface} = (\rho \Delta x \Delta y \Delta Z) \frac{DU}{Dt} \quad (4.4)$$

Body forces generally include gravity, centrifugal, Coriolis and electromagnetic forces; these all act on the volume from a distance.

Surface forces are those that act directly on the surface of a fluid element. These fluid forces include normal stress, in the x direction σ_{xx} , which is made up of pressure forces p exerted on the body and normal viscous stress components $\tau_{au_{xx}}$; and tangential stresses, τ_{xy} and τ_{xz} .

Summing these forces in the x direction, for a 2D fluid element we get:

$$\begin{aligned} \sum F_{surface,x} &= [\sigma_{xx} \Delta y \Delta z - (\frac{\delta \sigma_{xx}}{\delta x} \Delta x) \Delta y \Delta z] \\ &\quad + [(\tau_{xy} + \frac{\delta \tau_{yx}}{\delta y} \Delta y) \Delta x \Delta z - \tau_{yx} \Delta x \Delta z] \quad (4.5) \\ &= -\frac{\delta \sigma_{xx}}{\delta x} \Delta x \Delta y \Delta z + \frac{\delta \tau_{yx}}{\delta y} \Delta x \Delta y \Delta z \end{aligned}$$

Assuming that the fluid is Newtonian and isotropic, σ_{xx} can be related to pressure p and viscous stresses τ_{xx} by

$$\sigma_{xx} = -p + \tau_{xx}$$

For a Newtonian fluid, stress-strain relations can be described as

$$\tau_{xx} = 2\mu \frac{\delta u}{\delta x} \quad \tau_{yx} = \mu \frac{\delta u}{\delta y} \quad (4.6)$$

Where μ is the viscosity of the fluid. Combining equations 4.4 , 4.5 and 4.6 in the x direction, and cancelling out the volume term:

$$\rho \frac{Du}{Dt} = -\frac{\delta p}{\delta x} + \mu \left(\frac{\delta^2 u}{\delta x^2} + \frac{\delta^2 u}{\delta y^2} \right) + \rho \sum F_b \quad (4.7)$$

Here the acceleration term is the total derivative of u , defined as the combined local and advection inertial forces, which in two dimensions can be written as

$$\frac{Du}{Dt} = \frac{\delta u}{\delta t} + v \frac{\delta u}{\delta y} + u \frac{\delta u}{\delta x} \quad (4.8)$$

combining equations 4.7 and 4.8 and dividing through by ρ :

$$\underbrace{\frac{\delta u}{\delta t}}_{local\ acceleration} + v \underbrace{\frac{\delta u}{\delta y} + u \frac{\delta u}{\delta x}}_{convection} = - \underbrace{\frac{1}{\rho} \frac{\delta p}{\delta x}}_{pressure\ gradient} + \underbrace{\nu \left(\frac{\delta^2 u}{\delta x^2} + \frac{\delta^2 u}{\delta y^2} \right)}_{diffusion} + \underbrace{\sum F_b}_{body\ force} \quad (4.9)$$

Where ν is kinematic viscosity, defined as $\frac{\mu}{\rho}$.

4.1.3 Energy Conservation

Conservation of energy is derived from the first law of thermodynamics, that in a steady flow system the total energy of a control volume remains constant; that inflows and outflows must be equal. This can be expressed analogously to the mass conservation as

$$\frac{DE}{Dt} = \sum \dot{Q} + \sum \dot{W} \quad (4.10)$$

Where \dot{Q} is heat transfer and \dot{W} is the rate of work done. E is energy per unit mass and is expressed as

$E = C_p T$
 $\frac{DE}{Dt}$ can be expressed similarly to Equation 4.8:

$$\frac{DE}{Dt} = \frac{\delta E}{\delta t} + v \frac{\delta E}{\delta y} + u \frac{\delta E}{\delta x} = C_p \left(\frac{\delta T}{\delta t} + v \frac{\delta T}{\delta y} + u \frac{\delta T}{\delta x} \right) \quad (4.11)$$

For a 2D element, the total energy can therefore be calculated from

Figure 4.2: Flow of heat energy through a 2D element

Figure 4.3: water vapour moving through a 2D element

$$\rho \frac{DE}{Dt} \Delta x \Delta y = \rho C_p \left(\frac{\delta T}{\delta t} + v \frac{\delta T}{\delta y} + u \frac{\delta T}{\delta x} \right) \Delta x \Delta y \quad (4.12)$$

From Fourier's law of heat conduction, for a 2D system we can write

$$\dot{Q}_x = k A_x \frac{\delta T}{\delta x} = \dot{q}_x A_x = \dot{q}_x \Delta y \quad (4.13)$$

where \dot{q} is heat flux = \dot{Q}/A

The heat transferred into the element can thus be expressed as

$$[q_x + \frac{\delta q_x}{\delta x}] \Delta y - q_x \Delta y = \frac{\delta q_x}{\delta x} = k \frac{\delta^2 T}{\delta x^2} \Delta x \Delta y \quad (4.14)$$

reconstructing equation 4.10 with the inclusion of 4.14, considered also in the y direction, we can cancel out the volume term:

$$\underbrace{\frac{\delta T}{\delta t}}_{local acceleration} + u \underbrace{\frac{\delta T}{\delta x} + v \frac{\delta T}{\delta y}}_{convection} = \underbrace{k \left(\frac{\delta^2 T}{\delta x^2} + \frac{\delta^2 T}{\delta y^2} \right)}_{diffusion} \quad (4.15)$$

4.2 Humidity

One of the primary functions of the nasal cavity is the humidification of the incoming air in preparation for its interaction with the lungs. It therefore stands that any investigation into the fluid mechanisms of the nasal cavity would be incomplete without addressing the efficacy of this function. One simple but effective method for approximating humidification data in a computational domain is the use of the convection-diffusion equation.

Analogously to equations 4.15 and 4.9, for a 2D element we can write

$$\underbrace{\frac{\delta C_{H_2O}}{\delta t}}_{local acceleration} + u \underbrace{\frac{\delta C_{H_2O}}{\delta x} + v \frac{\delta C_{H_2O}}{\delta y}}_{convection} = D_{H_2O} \underbrace{\left(\frac{\delta^2 C_{H_2O}}{\delta x^2} + \frac{\delta^2 C_{H_2O}}{\delta y^2} \right)}_{diffusion} \quad (4.16)$$

Where C_{H_2O} is the concentration of water vapour and D_{H_2O} is the diffusivity of water in air.

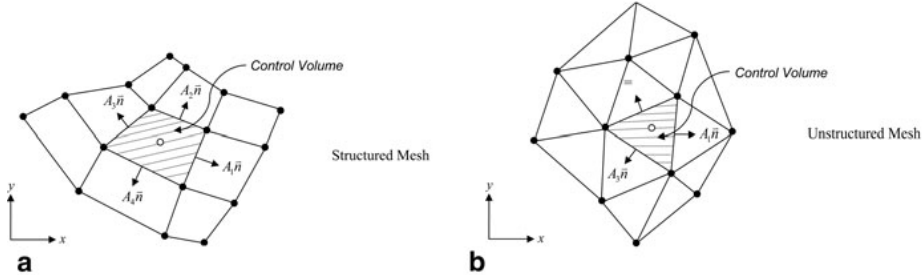


Figure 4.4: representation of mesh discretised with finite volume method

4.3 Solving the Governing Equations

The conservation equations outlined earlier in this chapter are nonlinear partial differential equations which, for complex domains such as the nasal cavity geometry, have no analytical solution; they must therefore be approximated algebraically and solved numerically.

4.3.1 Discretisation

Approximating, or discretising a system to make it numerically solvable can be done in many ways. One of the more common methods in modern solvers is the finite volume method, which can be applied to unstructured as well as structured meshes, making it particularly suited to complex geometries such as that of the nasal cavity.

The Finite Volume Method discretises the system into a series of volumes. The fluxes of relevant variables through the different faces of each element are then treated as a discrete system, which is able to be solved numerically.

Finite volume methods can tend to cause artificial, or numerical, diffusion if the mesh is of low quality. It is thus necessary to follow proper meshing practices, similar to those outlined in section 3.2.

4.3.2 Numerical Solution

Once the system has been discretised, a system of linear equations can be developed to describe the system. These equations can be solved with one of several methods. These methods can generally be divided into two categories: either direct or iterative. In general, for large complex domains such as the nasal cavity models presented in this paper, iterative methods are the only way to derive a solution.

4.4 Setup and Solution of Nasal Cavity Models Used in This Thesis

Here an overview will be given of the way that the solution of the nasal cavity systems presented in this thesis will be given. Firstly the models are prepared and meshed as discussed in the chapter 3. Once this is done the boundary conditions for the system must be defined.

The face and internal wall of the nasal cavity and pipe extension are set to no slip condition. This means that velocity is assumed to be zero on the surface of these zones. The exit of the pipe extension is given a constant velocity value calculated for each model as to give an inspiritory flow rate of 10 lpm, which has been suggested by the literature to be a realistic value for a resting flow rate. For these simulations this flow rate is treated as constant and the flow treated as steady, an assumption which greatly simplifies the solution process and one which is commonly used when comparing fluid flow characteristics between nasal cavity models (transient, or time dependant solutions are computationally much more costly).

The border of the hemispheric region around the face is set to atmospheric pressure. For resting inspiratory flow rates flows have been shown to be modeled most accurately as laminar; as such no turbulence model is used.

The numerical solution of the systems - described by the aforementioned boundary conditions and meshes - is approximated, for the models of this thesis, by the use of a commercial CFD code, in this case ANSYS FLUENT. The following chapter details the analysis of the solutions obtained for the five cavities.

Chapter 5

Results

5.1 Geometry Variations

One-hundred cross-sectional slices were taken from the nostrils tip to the nasopharynx. From nostrils tip to choanae, vertical slices were made, while angled slices were made in the nasopharynx until the slice became horizontal (Figure 5.3).

Figure 5.1 shows 8 coronal slices taken at equidistant spacing across the sagittal axis between the anterior vestibule and the nasopharynx. We see the airway elongate vertically which increases the perimeter but maintaining a relatively constant surface area. This area to perimeter ratio has been cited as an important factor in the development of fluid flow in the nasal cavity. The thinner cavities also tend to exhibit higher wall shear stress. This is because of the steeper velocity gradients, which create stress through the viscosity of air, near the wall. This narrowness is also likely to influence heat and vapour transfer in the cavities; when the cavities are narrower there is less distance for the heat and vapour to travel from the wall to saturate the incoming air, and so it is likely to saturate the airflow more comprehensively. The variation in cavity thickness between the cavities can also be clearly observed in this figure.

Figure 5.4 shows the cross sectional area as a function of normalised distance along the sagittal axis. The distance has been normalised between the entrance to the nostrils and the end of the nasopharynx. A sample of cavities from the pre-existing literature has also been included for comparison. A significant variation can be seen in the average cross sectional area of the models presented in this paper; This variation is most pronounced towards the rear of the cavities. None of the models show quite the same volume as the atrophic rhinitis model, also shown here as Garcia prior to the nasopharynx, although the 64yo is close. The general shape of the curve is reasonably similar for the various models in this paper, with notable exceptions in the Nasopharynx of the 64yo cavity and a larger spike in the vestibule region of the 78yo. Observations from Figure 3 can be compared with the cross sectional silhouettes from Fig-

ure 2, for a clearer understanding of the variations in geometry between the 4 models presented here. The range of cross-sectional areas allows us to observe the relationship between various fluid mechanical properties of the cavity and cavity volume/cross-sectional area.

Table 5.1 - 5.3 shows the variation of the volume, surface area and effective diameter respectively, in comparison with models from the literature. The volumes of the four models presented in this paper varied significantly. The largest discrepancies were noted in the pharynx and turbinate regions, with a less marked discrepancy in the vestibular region. The 48 yo is showing greater volume than that seen in the atrophic rhinitis patient from [9]. The surface area of the atrophic rhinitis model is also significantly lower, to the extent that the effective diameter, shown in Table 5.3, is larger than the models presented in this paper.

Minimal cross sectional area, shown in Table 5.4, is significant to flow across the cavity[4]. Here the atrophic rhinitis model shows larger minimal cross sectional area than any of those found in the models presented here, although it is quite close to that of the 64yo.

The circularity shape factor (a dimensionless quantity used in image analysis) was used to quantify the cross-sectional shape (Figure 5.5). The circularity, f_o , (also known as the isoperimetric quotient), is the ratio of cross-sectional area bounded by a closed curve, to its perimeter defined as,

$$f_o = \frac{4\pi A}{P^2}$$

At the nostril inlet, the circularity ranges from 0.18-0.30 and this reduces to a value of approximately = 0.035 (except the 64yo model). It then increases rapidly towards 1 where the two nasal chambers merge and form a single conduit in the form of the nasopharynx.

5.2 Pressure Drop

The pressure drops across the nasal cavities can also be seen in Figure 5.6 to vary in relation to the volume of the nasal cavity. This is in contrast to the experimental findings of [4, 3, 11], whos studies using rhinomanometry showed no significant decrease in pressure across the cavity to accompany the recorded variation in volume. The cause of this discrepancy is unclear. Here the pressure drop is primarily seen across the valve region. Here the nasopharynx has been excluded from the domain; the significant pressure drop across the nasopharynx was inversely proportional to the cross sectional areas of the respective nasal cavities

The pressure drops can be seen in Figure 5.5 to decrease in relation to the volume of the cavity. This fits well with the findings of previous experimental studies looking at pressure drops across nasal cavity models, as can be seen from the comparison with results from [9] and [45], both displayed in figure 5.5.

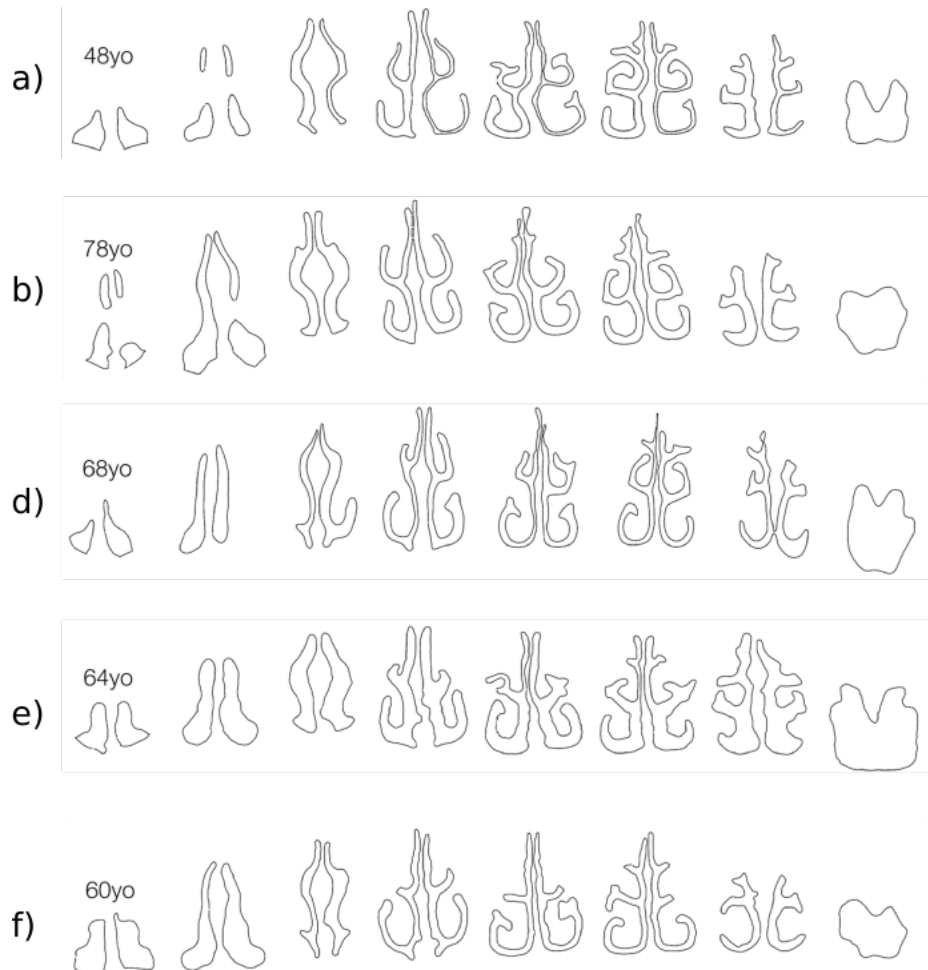


Figure 5.1: silhouettes of the cavities



Figure 5.2: Colour coded display of the regional divisions used in tables 5.1, 5.2, 5.3

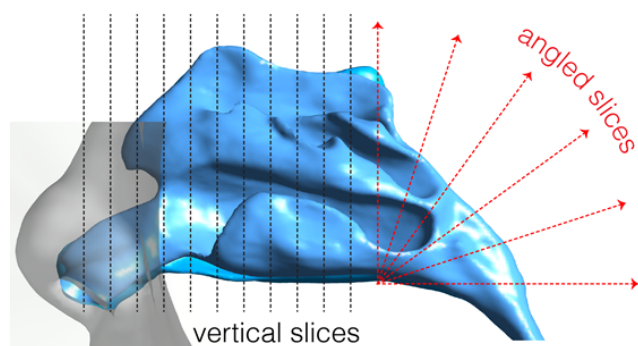


Figure 5.3: Representation of the slicing method used for sampling data across the sagittal axis throughout this thesis

	48yo	78yo	68yo	64yo	60yo	Xi al. [8]	Garcia et al.[9]
Turbinal region	18.54	22.78	24.62	30.722	16.73	12.63	33.66
Naso- pharynx	3.84	5.40	12.80	20.09	4.57	16.33	10.60
Vestibule	3.10	4.15	2.81	4.21	7.39	5.50	2.41
Total	25.48	32.33	40.23	55.07	28.69	34.43	47.77

Table 5.1: sectional volume, according to sections as seen in Figure 5.2 (cm^3)

	48yo	78yo	68yo	64yo	60yo	Xi al.	Garcia et al.
Turbinal region	170.92	174.07	190.44	163.44	138.80	112.59	133.50 ¹
Naso- pharynx	12.20	12.80	25.23	40.42	11.37	40.93	31.46
vestibule	15.71	17.37	12.45	17.92	46.96	35.58	-
total	198.82	204.25	228.11	221.79	197.192	189.10	164.96

Table 5.2: sectional surface area, according to sections shown in Figure 5.2(cm^2)

	48yo	78yo	68yo	64yo	60yo	Xi al.	Garcia et al.
Turbinal region	0.434	0.52	0.52	0.75	0.48	0.45	1.11
Naso- pharynx	1.26	1.69	2.03	1.99	1.61	1.60	1.35
vestibule	0.79	0.96	0.90	0.94	0.63	0.62	-
total	0.51	0.63	0.71	0.99	0.58	0.72	1.13

Table 5.3: Effective diameter $d_{eff} = \frac{4v}{a}$ (cm)

	48yo	78yo	68yo	64yo	60yo	Xi al.	Garcia et al.
MCA	1.665	3.0174	1.80	4.14	2.7	Unknown	3.04

Table 5.4: Minimal axial cross sectional area (cm^2)

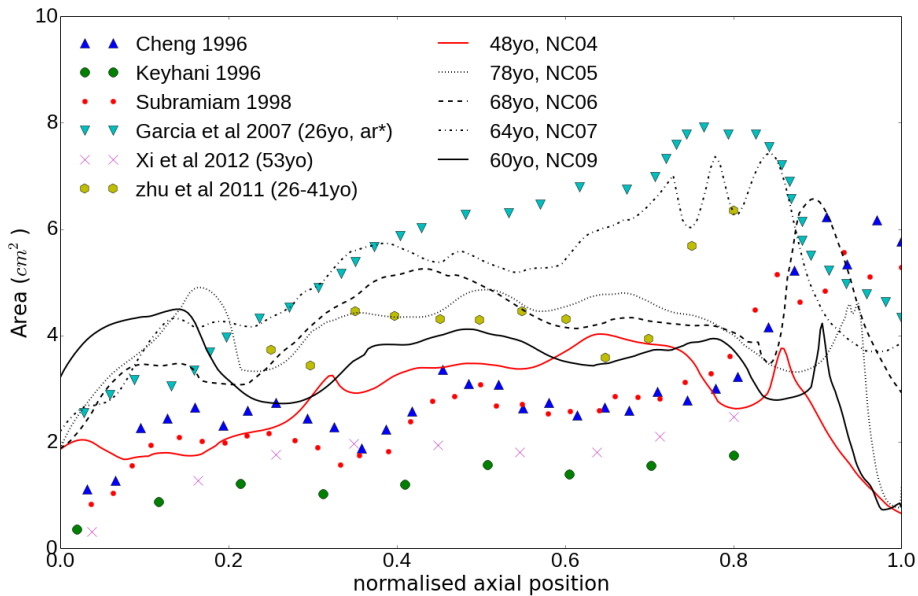


Figure 5.4: area versus distance across the four nasal cavities with a series of examples from the literature

flowrate (ml/s)	150	300	450	600
48yo	6.80	17.38	34.49	57.99
60yo	3.02	10.11	21.33	36.50
78yo	3.98	13.08	26.32	43.28
68yo	1.58	5.01	9.67	15.36
64yo	0.31	0.93	1.73	2.67
Inthavong et al 2014	5.87	20.23	43.04	73.95
Kelly et al 2004	7.79	22.51	44.11	71.89
Wen et al 2008	4.85	14.87	30.46	51.29
Weinhold et al. 2004	6.41	17.44	34.65	57.73
Garcia 2007 (AR patient)	4.19	11.69	22.43	36.03

Table 5.5: Variation of pressure drop with flow rate (m/s)

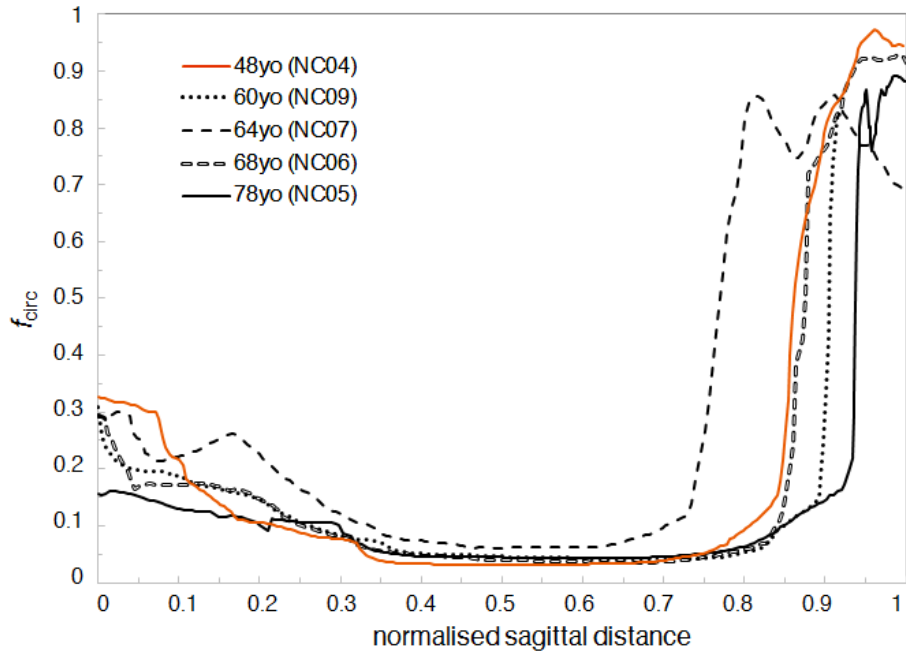


Figure 5.5: area to perimeter ratio variation with normalised length of the nasal cavity from the nostril inlet to the nasopharynx. This length for each model is: 48yo 8.97cm; 60yo 9.26cm; 64yo 9.60cm; 68yo 9.31cm; 78yo 8.45cm

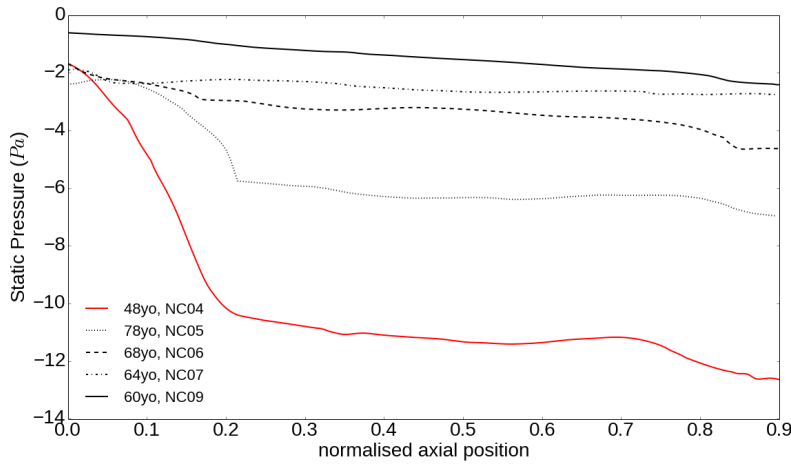


Figure 5.6: area versus distance across the four nasal cavities with a series examples from the literature

5.3 Wall Shear Stress and velocity

Figure 5.10 shows flow streamlines through the left and right nasal chambers with the chambers wall shear stress. In all the models flow acceleration and high wall shear stresses were consistently found in the region between the nasal vestibule entrance (anterior) and before the middle nasal passage. We also note that there is a preference for the streamlines to pass through the mid-height of the nasal chambers. A small fraction reached the olfactory region, and some inferiorly along the floor of the chambers. The highest wall shear stress values were found in the 48yo, 60yo, and 78yo models which are also the models with the smaller cross-sectional area profiles (from Figure 5.4), and corresponds to the highest velocity magnitudes produced by the streamlines in the models. Wall shear stress contours viewed from the top and lateral left-chamber side of all nasal models are shown in Figure 5.7. By using the same colour scale the results show directly the disparity between nasal models.

Figure 5.7 shows the wall shear stress across the five models presented in this paper. The valve region can be seen to be a region of particularly high wall shear across all the models. Also note that the locations of high wall shear vary significantly in the more voluminous cavities

From Figure 5.8, Wall shear stress can be seen to be more pronounced in general in the more voluminous models such as the 48yo, and in particular this effect is exaggerated in the valve region. Here the wall shear stress is mapped from the nostrils to the entrance to the nasopharynx. The nasopharynx showed more pronounced variations, in particular the 48yo showed a significant spike in wall shear stress in the nasopharynx, which is to be expected because of its lower cross sectional area. Note that the sagittal distribution of wall shear stress is much more even in the larger cavities. The valve region - considered of particular significance to the development of flow features within the nasal cavity [4] shows significant variation in wall shear stress concentration, with the 64yo and 60yo presenting a very even distribution of wall shear stress, in contrast to the 48yo or 78yo which show wall shear more pronounced around the opening from the vestibule. Similar variations can also be seen in the distribution within the turbinal region (Figure 5.7).

Cross-sections at the internal nasal valve, and turbinate region were taken for each model and its velocity contour presented in Figure 5.9. We traced the perimeter of each cross-section starting from its apex and follow down in a counter-clockwise direction. For the nasal valve cross-section in all models, we found that the surface proportion was distributed almost evenly between the lateral and septum walls, since its partition occurred at 0.5. For the turbinate region, this value was 0.7 meaning that 70% of the perimeter resides along the lateral side and 30% of the perimeter is along the septum wall. For the 48yo model we labelled three peaks for the nasal valve slices (r_1 , r_2 , and l_1) to help identify the locations on the cross-section itself.

Wall shear stress peaks occurred close to the regions of maximum velocities in the contours. Superiorly, where the velocity is very low, the wall shear stress is nearly zero. These peaks and troughs correlate well with the contour slices

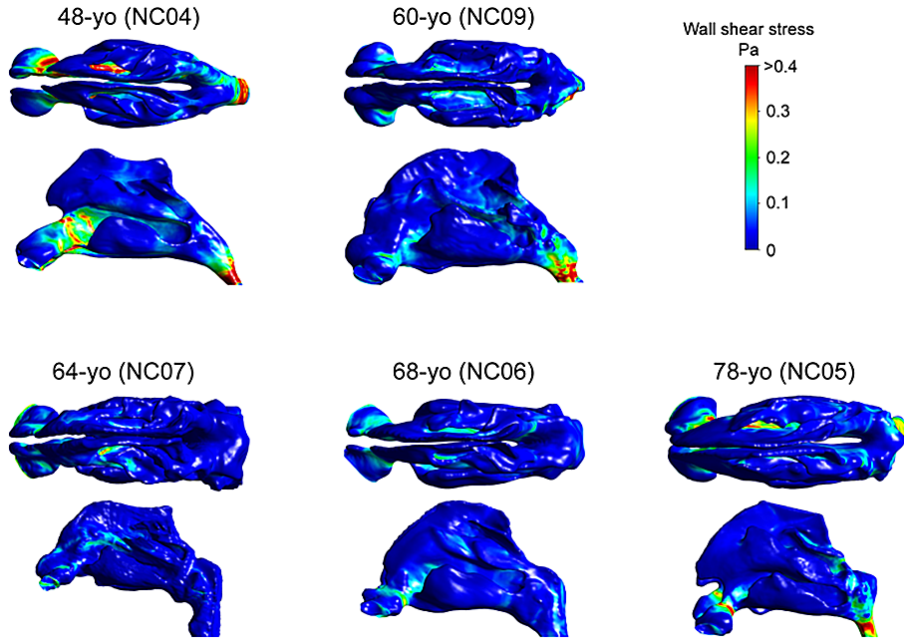


Figure 5.7: Direct comparison of WSS surface contours between all models

and is consistent for all models.

5.4 Heat and Vapour Transfer

Some variation in the heat and vapour transfer efficacy can be seen between the models presented in this thesis. Note the higher than average figures for temperature and h₂o mass fraction in the valve area of the 78yo. In general the more voluminous models exhibit lower humidity and temperature (Figures 5.11 and 5.12). The data from the atrophic rhinitis study by Garcia et al [9]; the humidity and temperature distribution in this model seem to be lower in proportion to the increased voluminousness of this model (see figure 5.4).

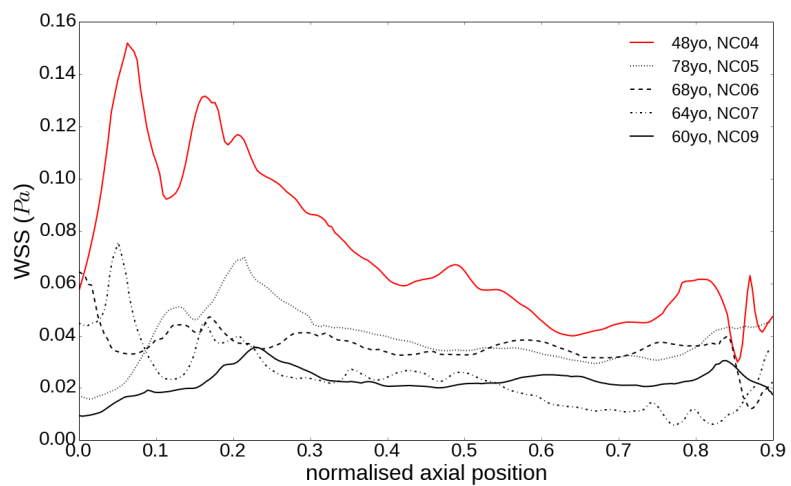
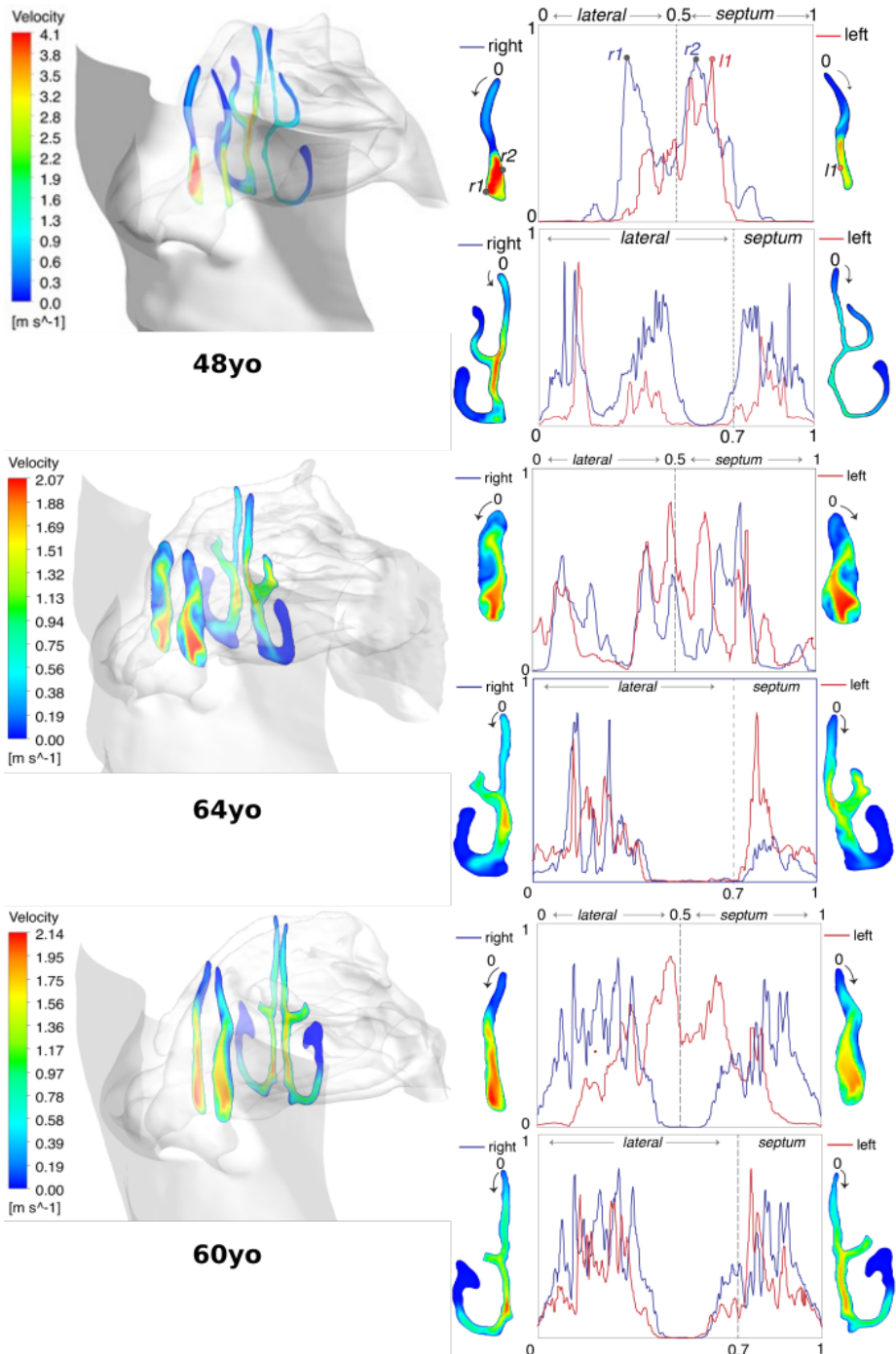


Figure 5.8: coronal area weighted average of wall shear stress plotted as a function of distance from the entrance to the cavity across the saggital axis



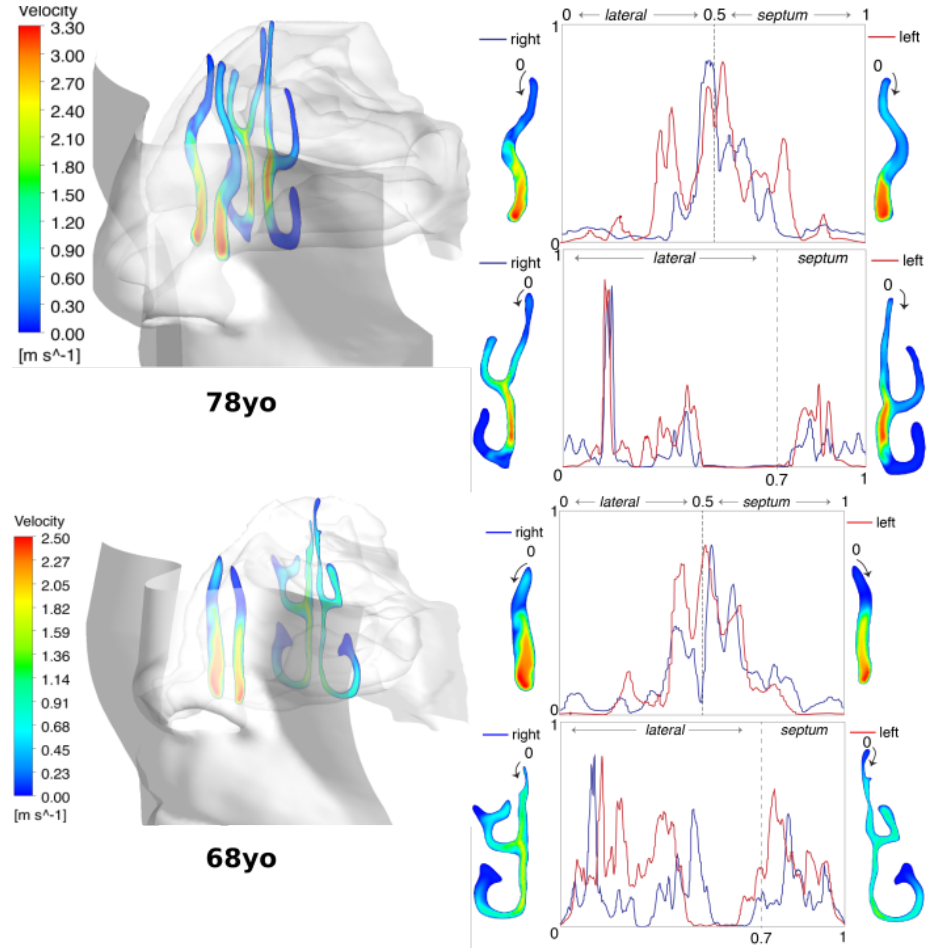
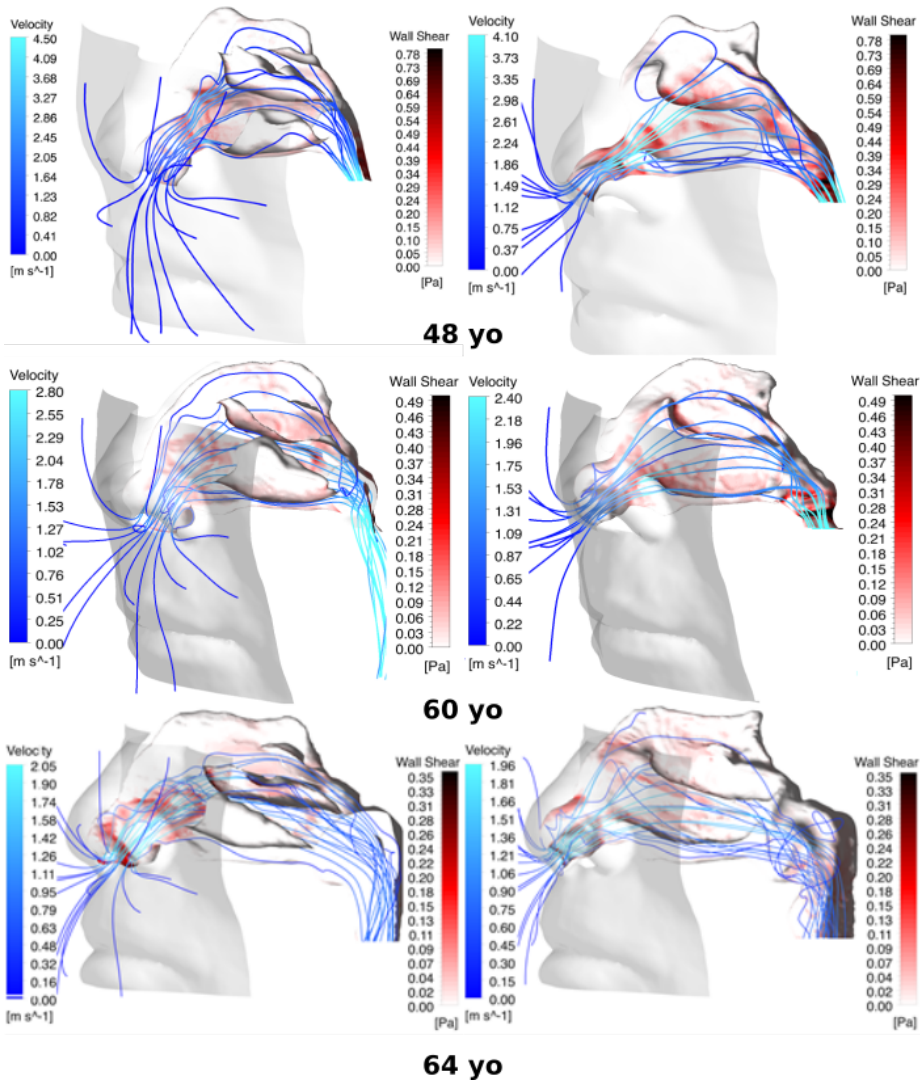


Figure 5.9: Velocity contours and wall shear stress values along the perimeter outlines of two cross-sections. The x-axis is the perimeter distance starting from the top apex of each cross-section slice, and moves along the perimeter laterally. One full tracing around the perimeter is defined as 1.0. The dashed line represents the floor of the cross-section opposing its apex, and for the nasal valve, the halfway point 0.5, while for the turbinate cross-section it is 0.7. The y-axis represents normalized wall shear stress 0 – 1.



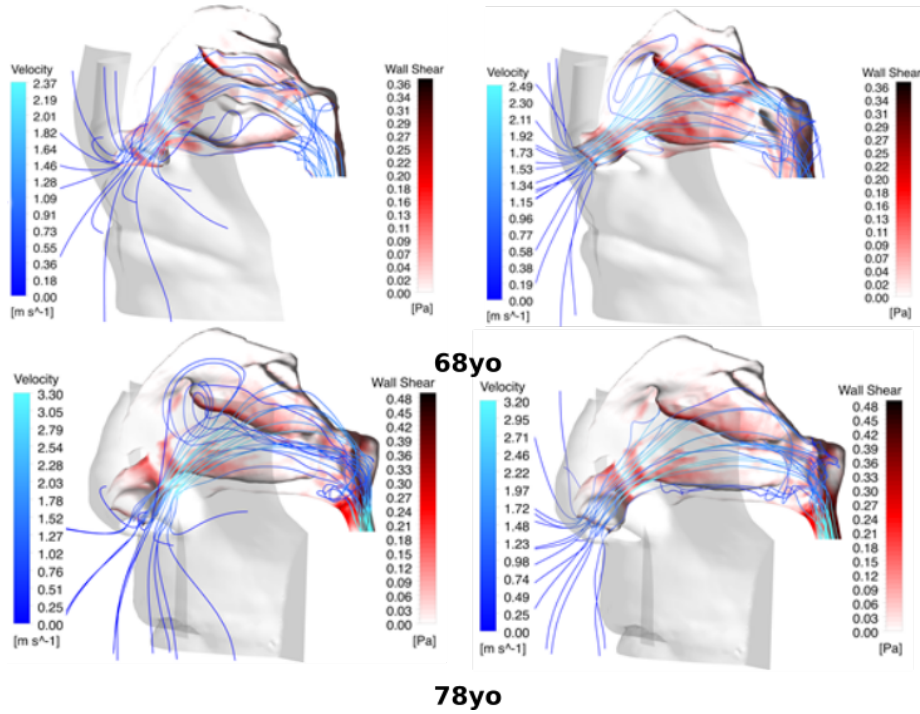


Figure 5.10: Flow streamlines (coloured in blue) passing through the left and right chambers of the nasal cavity. Each chambers wall shear stress is shown (coloured in red).

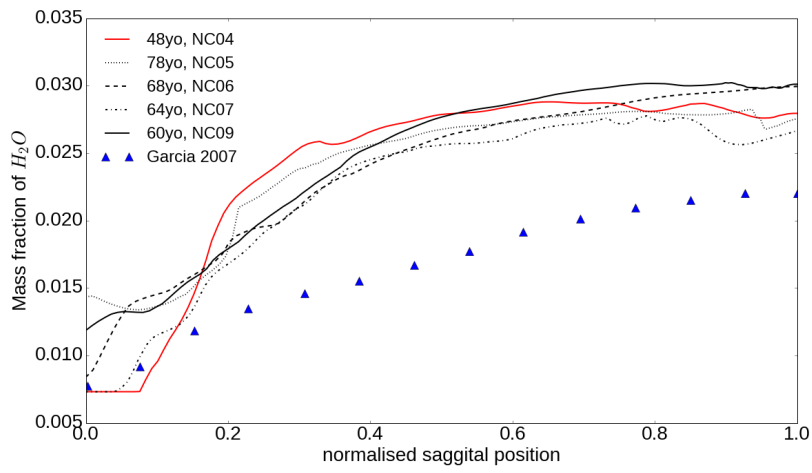


Figure 5.11: average mass fraction of H_2O as a function of normalised saggital position

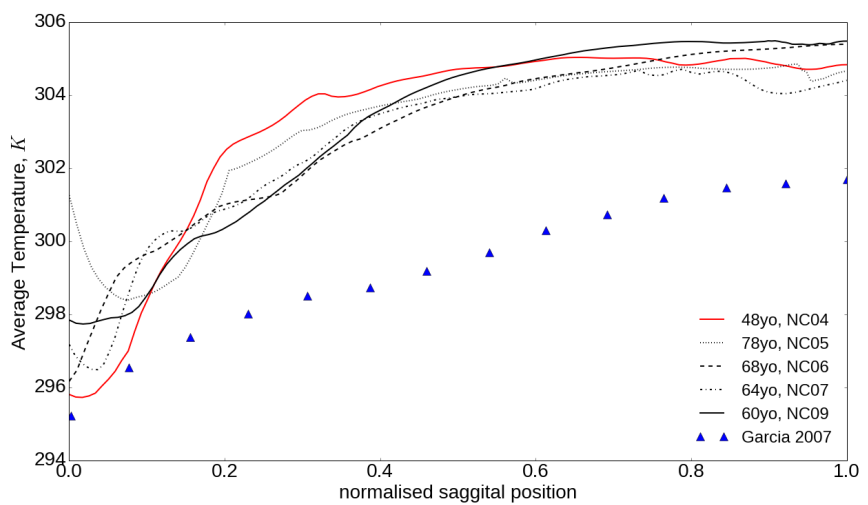


Figure 5.12: average ambient temperature as a function of normalised saggital position

Chapter 6

Discussion

Evaluation of nasal respiratory function for diagnostic or research purposes relies on categorisation of an individual's demographics, including age, gender, and ethnicity. It is known that normal changes in inter- or intra-individual nasal cavities manifest through age. This is especially true of intranasal volume, which is thought to increase due to hormonal changes leading to mucosal atrophy[6, 13]. Edelstein[3] and Lindemann et al.[4] found correlations between aging and the occurrence of a range of rhinological conditions (e.g. dry cold itchy noses; crusting, postnasal dripping and obstructed nasal breathing) although their association with nasal morphology was not established. Thus, a detailed analysis of the nasal morphology and its effect on respiratory function in older adult patients may contribute towards this understanding.

Demographic factors such as age, gender, and ethnicity play an important role in determining ones nasal anatomy and physiology. For example, it was found that males exhibited larger nasal cavities e.g. larger normal pharyngeal areas in males over females[46, 47]. However, very few studies have quantified these differences. In terms of geographic variations with age, Kalmovich, et al.[6] found a significant increase in nasal cavity volume and minimal cross sectional area with age using acoustic rhinometry on 165 patients. Later, Lindemann, et al.[13] used acoustic rhinometry in conjunction with rhinomanometry and validated questionnaires to survey the nasal cavities of eighty patients. While the questionnaire and rhinomanometry did not show any difference between the older and younger subjects, a marked increase in the volume of the nasal cavity with age was found from the acoustic rhinometry data. More recently, Loftus, et al.[12] found higher intranasal volumes with age on CT volumetric analysis.

In the past, quantifying differences in nasal airflow has been limited by a lack of sensitive tools that can quantify the complexities of the sinonasal cavity. More recently, CFD has been proven to be a useful tool for detailed analysis of nasal airflow. With this new tool, normative data based on demographics is required so that these can be compared with disease states. We aimed at investigating the nasal airflow anatomy and physiology of older Chinese adult males to understand geometry features and dynamics of inhaled flow field in

this specific demographic group.

Our geometry analyses revealed the significant influence of the area to perimeter ratio on fluid flow development in the nasal cavity. The thinner cavities exhibited higher wall shear stresses due to sharper velocity gradients that were produced. The narrow geometry would also increase heat and vapour transfer as there is less distance for the heat energy and vapour to transport from the wall to condition the inhaled air.

The cross-sectional area of slices taken along the nasal cavity, provided insight into the patients airway patency based on the degree of openness of the nasal chamber. These observations (from Figure 5.4) can be compared with cross sectional outlines in Figure 5.1 which allow predictions of the likely relationships between fluid flow properties caused by the individual nasal geometry features.

A shape factor in the form of the circularity, described the overall shape of each cross-sectional slice along the nasal cavity geometry. A circularity of 1 implies a circular shape, although this can be masked by irregular shapes that coincidentally have the same values as a smooth circle. A value close to zero, however is more definite providing a strong suggestion of a jagged and non-circular shape. The sharp increase in the circularity plot indicated where merging of the two chambers occurs. The circularity is a well-established measurement commonly used in image analysis of particles, and this is the first time it has been applied for shape detection in nasal cavity geometries. The results in this study showed that circularity is useful as an indicator and quantifiable metric for identifying the anterior, middle, and posterior nasal cavity regions.

Fluid flow analysis showed the relationship between inhaled fluid dynamics and its impact on nasal sensation in the form of fluid-surface shear. Regions of high acceleration were often caused by the airway converging into a smaller cross-section thereby accelerating the flow through. This corresponded with a high wall shear stress region in the vicinity of the minimised cross-section. The results showed that the middle region partition in this study incorporated the minimum cross-sectional area into its region, which is known to occur around the nasal valve, although it could be considered as part of the anterior nasal cavity.

The 48yo and 60yo models were the smallest in size and this resulted in higher wall shear stress magnitudes. Based on the geometry analysis, peak velocities and wall shear stresses should occur at the minimal cross-sections, and this corroborated well with the highest values indeed found in the 48yo and 60yo models. Locally, the highest wall shear stress concentrations occurred around the internal nasal valve, and this is consistent across all the models. Interestingly the nasopharynx also exhibited a significant increase in wall shear stress, and this was due to the cross-sectional area decreasing at the nasopharynx.

The wall shear stress profiles along cross-sectional slices showed peak wall shear stresses produced inferiorly on the internal nasal valve while there was very low wall shear stresses superiorly. For the turbinate slices, the velocity contours showed the bulk flow and peak velocity were offset from the nasal floor. This is the continuation of the fluid flow that was rising from the nasal

valve region. The main nasal passage expands but the flow is unable to reach the new extremities.

The static pressure variation shown in figure 5.6 merits some discussion. Although it would seem logical that an increased cavity volume would have the effect of reducing pressure drop, this is not the result that has been recorded by previous researchers using rhinomanometry [4]. This discrepancy is possibly due to the flexibility of the nasopharynx, varying the diameter of the exit in ways that are not replicated in the ct models.

The more even distribution of wall shear stress - both sagittally, as seen in Figures 5.7 and 5.8; and coronally, as seen in Figure 5.9 - is indicative of variations in airflow structure and therefore performance of the nasal cavity models. In particular the variation in the local maxima for WSS found in the region of the nasal valve is indicative of varying air conditioning capacity.

It seems in particular that it is only in the more severely enlarged cavities that drastically increased vorticity is seen in the air flow structures. The volume of the NC07 model of 55.07 cm^3 .

It seems probable that these marked increases in vorticity are linked to the observed reductions in air-conditioning functionality in specimens from this age group [48]. This is in accordance with the findings of [9] in relation to atrophic rhinitis patients. The model in their study had a recorded volume of 34.5 cm^3 , however this was only measured to the end of the septum, and a comparison with the models from this study, as seen in figure 5.4 shows that the volume through the turbinal region of the atrophic rhinitis model was significantly larger than that of the largest model from this study, NC07. Although a quantity is not given for the volume of the nasopharynx in the atrophic rhinitis model, qualitative comparison between the images of the model and those of the models from this study seem to show that the significant expansion of the nasopharynx which is present in all of the elderly models was not present in the model of the younger (26 yo) atrophic rhinitis sufferer.

previous research has suggested that the presence of significant vortices such as those seen in the larger of the models presented in this study is related to the impairment of air conditioning functionality. The specifics of this mechanism, however, are yet to be investigated, and this is a piece of work which should be completed in future. In addition, the impact of the observed variations in airflow structure on the ability of the nasal cavity to filter particles from the air has not been investigated, and this is also an area which could be of some significance.

The heat and vapour transfer figures show what seems to be close to an inverse linear relationship between the voluminousness of the cavities and their heat and vapour transfer efficacy. This is particularly pronounced in the nasal valve. This relationship agrees well with the data from Garcia et al [9] taken from their atrophic rhinitis patient. This suggests that the mechanisms causing this reduced efficacy in the atrophic rhinitis patient are the same as those in elderly patients; this may imply that, for more extreme cases, that the surgical procedures implemented for atrophic rhinitis patients could also be effective for the elderly. It has been suggested by [4] that heat and vapour transfer are

significantly effected by the minimal cross sectional area. The current data doesn't show anything to support or disprove this suggestion, as in general the models presenting higher mcas are also presenting higher voluminousness. In fact, the model that shows the highest MCA relative to its voluminousness [NC09], shows very good heat and vapour transfer.

Detailed understanding of the associations among variabilities in nasal anatomy, age, and airflow dynamics will greatly improve current knowledge regarding the influence of conductive mechanisms on olfactory ability. Variabilities in nasal anatomy have traditionally been understood to influence olfaction[49, 50]. Nasal profiles that have been postulated to be associated with improved olfaction include the dorsal conduit, which delivers inhaled odorant-laden air to the olfaction recess through enhanced olfactory airflow, and an enlarged olfactory recess at the posterior end of the nasal cavity[49, 50, 51]. It has also been reported that anatomical changes in the olfactory cleft or the nasal valve region alter odorant transport to the olfactory epithelium[52]. Furthermore, the incidence of olfactory dysfunction in the general population is unclear, but has been estimated to be between 1% and 3%, with an exponential increase of 24.5% among individuals aged 53 to 97 years[53, 54, 55, 56, 57]. The present study provides preliminary understanding connecting nasal anatomy, age and airflow dynamics together.

Chapter 7

Conclusion

Bibliography

- [1] Jie Tan, Demin Han, Jie Wang, Ting Liu, Tong Wang, Hongrui Zang, Yunchuan Li, and Xiangdong Wang. Numerical simulation of normal nasal cavity airflow in chinese adult: a computational flow dynamics model. *European Archives of Oto-Rhino-Laryngology*, 269(3):881–889, 2012.
- [2] Jian Wen, Kiao Inthavong, Jiyuan Tu, and Simin Wang. Numerical simulations for detailed airflow dynamics in a human nasal cavity. *Respiratory Physiology & Neurobiology*, 161(2):125–135, 2008.
- [3] David R. Edelstein. Aging of the normal nose in adults. *The Laryngoscope*, 106(S81):1–25, 1996.
- [4] Joerg Lindemann, Diana Sannwald, and Kerstin Wiesmiller. Age related changes in intranasal air conditioning in the elderly. *Laryngoscope*, 118:1472–1475, 2008.
- [5] James Ho, Kwok Chan, Wayne Hu, Wah Lam, Ling Zheng, George Tipoe, June Sun, Raymond Leung, and Kenneth Tsang. The effect of aging on nasal mucociliary clearance, beat frequency, and ultrastructure of respiratory cilia. *American Journal of Respiratory and Critical Care Medicine*, 163(4):983–988, Mar 2001.
- [6] L. M. Kalmovich, D. Elad, U. Zaretsky, A. Adunsky, A. Chetrit, S. Sadetzki, S. Segal, and M. Wolf. Endonasal geometry changes in elderly people: Acoustic rhinometry measurements. *Journals of Gerontology Series a-Biological Sciences and Medical Sciences*, 60:396–398, 2005.
- [7] Victoria E Varga-Huettner and Jayant M Pinto. Physiology of the aging nose and geriatric rhinitis. In *Nasal Physiology and Pathophysiology of Nasal Disorders*, pages 165–181. Springer, 2013.
- [8] Jinxiang Xi, Ariel Berlinski, Yue Zhou, Bruce Greenberg, and Xiawei Ou. Breathing resistance and ultrafine particle deposition in nasal-laryngeal airways of a newborn, an infant, a child, and an adult. *Annals of Biomedical Engineering*, 40:2579–2595, 2012.

- [9] Guilherme J. M. Garcia, Neil Bailie, Dario A. Martins, and Julia S. Kimbell. Atrophic rhinitis: a cfd study of air conditioning in the nasal cavity. *Journal of Applied Physiology*, 103(3):1082–1092, 2007.
- [10] Jian Hua Zhu, Heow Pueh Lee, Kian Meng Lim, Shu Jin Lee, and De Yun Wang. Evaluation and comparison of nasal airway flow patterns among three subjects from caucasian, chinese and indian ethnic groups using computational fluid dynamics simulation. *Respiratory Physiology & Neurobiology*, 175(1):62–69, 2011.
- [11] Si Whan Kim, Ji-Hun Mo, Jeong-Whun Kim, Dong-Young Kim, Chae-Seo Rhee, Chul Hee Lee, and Yang-Gi Min. Change of nasal function with aging in korean. *Acta Oto-Laryngologica*, 127(S558):90–94, 2007.
- [12] Patricia A Loftus, Sarah K Wise, Daniel Nieto, Nicholas Panella, Ashley Aiken, and John M DelGaudio. Intranasal volume increases with age: Computed tomography volumetric analysis in adults. *The Laryngoscope*, 2016.
- [13] Joerg Lindemann, Evangelia Tsakiroglou, Iordanis Konstantinidis, and Kerstin Lindemann. Normal aging does not deteriorate nose-related quality of life: Assessment with nose and snot-20 questionnaires. *Auris Nasus Larynx*, 37:303–307, 2010.
- [14] H Stammberger. History of rhinology: anatomy of the paranasal sinuses. *Rhinology*, 27(3):197–210, 1989.
- [15] R. Eccles. Nasal airflow in health and disease. *Acta Oto-Laryngologica*, 120(5):580–595, 2000.
- [16] O. Hilberg, A. C. Jackson, D. L. Swift, and O. F. Pedersen. Acoustic rhinometry: evaluation of nasal cavity geometry by acoustic reflection. *JOURNAL OF APPLIED PHYSIOLOGY*, 66:295–303, 1989.
- [17] D. J. Doorly, D. J. Taylor, and R. C. Schroter. Mechanics of airflow in the human nasal airways. *Respiratory Physiology & Neurobiology*, 163(13):100–110, 2008.
- [18] Baoshun Ma, Vincent Ruwet, Patricia Corieri, Raf Theunissen, Michel Riethmuller, and Chantal Darquenne. Cfd simulation and experimental validation of fluid flow and particle transport in a model of alveolated airways. *Journal of Aerosol Science*, 40(5):403–414, 2009. doi: DOI: 10.1016/j.jaerosci.2009.01.002.
- [19] J. Tu, G.H. Yeoh, and C. Liu. *Computational fluid dynamics: a practical approach*. Butterworth-Heinemann, 2008.
- [20] K Keyhani, PW Scherer, and MM Mozell. Numerical simulation of airflow in the human nasal cavity. *Journal of biomechanical engineering*, 117(4):429–441, 1995.

- [21] J.F. Wendt and J.D. Anderson. *Computational fluid dynamics: an introduction*. Springer, 2009.
- [22] I. Hahn, P.W. Scherer, and M.M. Mozell. Velocity profiles measured for airflow through a large-scale model of the human nasal cavity. *J Appl. Physiol.*, 75(5):2273–2287, 1993.
- [23] T. B. Martonen, Z. Zhang, G. Yue, and C. J. Musante. 3-d particle transport within the human upper respiratory tract. *Journal of Aerosol Science*, 33(8):1095–1110, 2002.
- [24] H. Shi, C. Kleinstreuer, and Z. Zhang. Laminar airflow and nanoparticle or vapor deposition in a human nasal cavity model. *Journal Biomech. Eng.*, 128(5):697–706, 2006.
- [25] G. Xiong, J. Zhan, K. Zuo, J. Li, L. Rong, and G. Xu. Numerical flow simulation in the post-endoscopic sinus surgery nasal cavity. *Medical and Biological Engineering and Computing*, 46(11):1161–1167, 2008.
- [26] Joerg Lindemann, Hans-Juergen Brambs, Tilman Keck, Kerstin M. Wiesmiller, Gerhard Rettinger, and Daniela Pless. Numerical simulation of intranasal airflow after radical sinus surgery. *American Journal of Otolaryngology*, 26(3):175–180, 2005. doi: DOI: 10.1016/j.amjoto.2005.02.010.
- [27] Qin Jiang Ge, Kiao Inthavong, and Ji Yuan Tu. Local deposition fractions of ultrafine particles in a human nasal-sinus cavity cfd model. *Inhalation Toxicology*, 24(8):492–505, 2012.
- [28] R Martin, PS Vig, and DW Warren. Nasal resistance and vertical dento-facial features. In *Journal of Dental Research*, volume 60, pages 539–539, 1981.
- [29] Andreas Lintermann, Matthias Meinke, and Wolfgang Schrder. Fluid mechanics based classification of the respiratory efficiency of several nasal cavities. *Computers in Biology and Medicine*, 43(11):1833 – 1852, 2013.
- [30] Kiao Inthavong, Man Chiu Fung, Xuwen Tong, William Yang, and Jiyuan Tu. High resolution visualization and analysis of nasal spray drug delivery. *Pharmaceutical research*, pages 1–8, 2014.
- [31] D. J. Taylor, D. J. Doorly, and R. C. Schroter. Inflow boundary profile prescription for numerical simulation of nasal airflow. *Journal of The Royal Society Interface*, 7:515–527, 2010.
- [32] M.A. Burgos, E. Sanmiguel-Rojas, A. Martn-Alcntara, and M.L Hidalgo-Martnez. Effects of the ambient temperature on the airflow across a caucasian nasal cavity. *International Journal for Numerical Methods in Biomedical Engineering*, 30(3):430–445, 2014.

- [33] Jinxiang Xi, JongWon Kim, Xiuhua A. Si, Wei Chung Su, and Yue Zhou. Effects of the facial interface on inhalation and deposition of micrometer particles in calm air in a child airway model. *Inhalation Toxicology*, 26:492–505, 2014.
- [34] Sven Ingelstedt and Nils Gunnar Toremalm. Air flow patterns and heat transfer within the respiratory tract: A new method for experimental studies on models. *Acta Physiologica Scandinavica*, 51(2-3):204–217, 1961.
- [35] ML Nuckols, JL Zumrick, and CE Johnson. Heat and water vapor transport in the human upper airways at hyperbaric conditions. *Journal of biomechanical engineering*, 105(1):24–30, 1983.
- [36] David Elad, Michael Wolf, and Tilman Keck. Air-conditioning in the human nasal cavity. *Respiratory Physiology & Neurobiology*, 163(1-3):121 – 127, 2008. Respiratory Biomechanics.
- [37] T. Keck, R. Leiacker, A. Heinrich, S. Kuhneman, and G. Rettinger. Humidity and temperature profiles in the nasal cavity. *Rhinology*, 38(167-171), 2000.
- [38] J. Lindemann, T. Keck, K. Wiesmiller, B. Sander, H.J. Brambs, G. Rettinger, and P. Pless. A numerical simulation of intranasal air temperature during inspiration. *The Laryngoscope*, 114:1037–1041, 2004.
- [39] S. Naftali, R.C. Schroter, J. Shiner, and D. Elad. Transport phenomena in the human nasal cavity: A computational model. *Annals of Biomedical Engineering*, 26:831–839, 1998.
- [40] David Elad, Sara Naftali, Moshe Rosenfeld, and Michael Wolf. Physical stresses at the air-wall interface of the human nasal cavity during breathing. *Journal of Applied Physiology*, 100(3):1003–1010, 2006.
- [41] S. Naftali, M. Rosenfeld, M. Wolf, and D. Elad. The air-conditioning capacity of the human nose. *Annals of Biomedical Engineering*, 33:545–553, 2005.
- [42] Corbin D Sullivan, Guilherme JM Garcia, Dennis O Frank-Ito, Julia S Kimbell, and John S Rhee. Perception of better nasal patency correlates with increased mucosal cooling after surgery for nasal obstruction. *Otolaryngology—Head and Neck Surgery*, pages 139–47, 2013.
- [43] Shen Yu, Xiu-zhen Sun, and Ying-xi Liu. Numerical analysis of the relationship between nasal structure and its function. *The Scientific World Journal*, 2014.
- [44] I. Weinhold and G. Mlynški. Numerical simulation of airflow in the human nose. *European Archive Otorhinolaryngology*, 261:452–455, 2004.

- [45] J.T. Kelly, B. Asgharian, J.S. Kimbell, and Wong. B.A. Particle deposition in human nasal airway replicas manufactured by different methods. part 1: Inertial regime particles. *Aerosol Science and Technology*, 38(11):1063–1071, 2004.
- [46] J. Huang, H. Shen, M. Takahashi, T. Fukunaga, H. Toga, K. Takahashi, and N. Ohya. Pharyngeal cross-sectional area and pharyngeal compliance in normal males and females. *Respiration*, 65(6):458–68, Nov 1998. Copyright - Copyright (c) 1998 S. Karger AG, Basel; Last updated - 2011-04-05.
- [47] Lee J Brooks and Kingman P Strohl. Size and mechanical properties of the pharynx in healthy men and women. *The American Review of Respiratory Disease*, 1992.
- [48] Joerg Lindemann, Evangelia Tsakiroglou, Tilman Keck, Richard Leiacker, and Kerstin M. Wiesmiller. Nasal air conditioning in relation to acoustic rhinometry values. *American Journal of Rhinology & Allergy*, 23(6):575–7, 11 2009. Copyright - Copyright OceanSide Publications Nov 2009; Last updated - 2012-03-03.
- [49] Thomas P Eiting, J Blair Perot, and Elizabeth R Dumont. How much does nasal cavity morphology matter? patterns and rates of olfactory airflow in phyllostomid bats. *Proceedings of the Royal Society of London B: Biological Sciences*, 282(1800):20142161, 2015.
- [50] Brent A Craven, Thomas Neuberger, Eric G Paterson, Andrew G Webb, Eleanor M Josephson, Edward E Morrison, and Gary S Settles. Reconstruction and morphometric analysis of the nasal airway of the dog (*canis familiaris*) and implications regarding olfactory airflow. *The Anatomical Record*, 290(11):1325–1340, 2007.
- [51] Thomas P Eiting, Timothy D Smith, J Blair Perot, and Elizabeth R Dumont. The role of the olfactory recess in olfactory airflow. *Journal of Experimental Biology*, 217(10):1799–1803, 2014.
- [52] Kai Zhao, Peter W. Scherer, Shoreh A. Hajiloo, and Pamela Dalton. Effect of anatomy on human nasal air flow and odorant transport patterns: Implications for olfaction. *Chem. Senses*, 29(5):365–379, 2004.
- [53] B N Landis, C G Konnerth, and T Hummel. A study on the frequency of olfactory dysfunction. *The Laryngoscope*, 114(10):1764–1769, 2004.
- [54] Annika Brämerson, Leif Johansson, Lars Ek, Steven Nordin, and Mats Bende. Prevalence of olfactory dysfunction: The skövde population-based study. *The Laryngoscope*, 114(4):733–737, 2004.
- [55] Charles J Wysocki and Avery N Gilbert. National geographic smell survey: effects of age are heterogenous. *Annals of the New York Academy of Sciences*, 561(1):12–28, 1989.

- [56] Howard J Hoffman, Erick K Ishii, and Robert H Macturk. Age-related changes in the prevalence of smell/taste problems among the united states adult population: Results of the 1994 disability supplement to the national health interview survey (nhis). *Annals of the New York Academy of Sciences*, 855(1):716–722, 1998.
- [57] Claire Murphy, Carla R Schubert, Karen J Cruickshanks, Barbara EK Klein, Ronald Klein, and David M Nondahl. Prevalence of olfactory impairment in older adults. *Jama*, 288(18):2307–2312, 2002.